

## **Nanostructures Technology, Research and Applications**

### **Academic and Research Staff**

Professor Karl Berggren, James M. Carter, Robert C. Fleming, Dr. Ralf Heilmann, Dr. Rajesh Menon, Mark. K. Mondol, Dr. Mark L. Schattenburg, and Professor Henry I. Smith,

### **Visiting Scientists and Research Affiliates**

Dr. Patrick N. Everett, Dr. James G. Goodberlet, Dr. Timothy Savas

### **Graduate Students**

Mireille Akilian, Will Arora, Tymon Barwicz, Cynthia Caramana, Chih-Hao Chang, David Chao, Lynn Chen, Chulmin Joo, Juan Montoya, Euclid Moon, Tom O'Reilly, Amil Patel, Minghao Qi, Sander Smits, Ryan Tabone, Mike Walsh, Feng Zhang

### **Collaborators**

Professor Leslie Kolodziejcki, Professor Caroline Ross, Professor Carl Thompson, Professor Rajeev Ram, Professor George Barbastathis, Solomon Assefa, Ytshak Avrahami, Reginald Bryant, Dr. Fernando Castano, Dr. Joy Cheng, Chris Dames, Amanda Giermann, Dr. Jane Guo, Jin In Hyun, Filip Ilievski, Wonjoon Jung, Yamini Kangude, Ramkumar Krishnan, Elizabeth Lyons, Eric Mattson, Ashok Rajamani, Sarah Rodriguez, Sheila Tandon

### **Technical and Support Staff**

James Daley, Cynthia Lewis

## **1. Nanostructures Laboratory**

The NanoStructures Laboratory (NSL) at MIT develops techniques for fabricating surface structures with feature sizes in the range from nanometers to micrometers, and uses these structures in a variety of research projects. The NSL is closely coupled to the Space Nanotechnology Laboratory (SNL) with which it shares facilities and a variety of joint programs. The NSL and SNL include facilities for lithography (photo, interferometric, electron-beam, and x-ray), etching (chemical, plasma and reactive-ion), liftoff, electroplating, sputter deposition, and e-beam evaporation. Much of the equipment, and nearly all of the methods, utilized in the NSL/SNL are developed in house. Generally, commercial lithography and processing equipment, designed for the semiconductor industry, cannot achieve the resolution needed for nanofabrication, is inordinately expensive, and lacks the required flexibility for our research. The research projects within the NSL/SNL fall into four major categories: (1) development of nanostructure fabrication technology; (2) nanoelectronics, nanomagnetism and microphotonics; (3) periodic structures for x-ray optics, spectroscopy, atomic interferometry and nanometer metrology; (4) building a bridge to macromolecular assembly and 3-dimensional structures via surface templating and membrane folding.

## 2. Scanning-Electron-Beam Lithography

### **Sponsors:**

National Science Foundation - DMR-9808941

Defense Advanced Research Projects Agency & U.S. Army Research Office –  
Grant DAAD19-99-1-0280

### **Project Staff:**

Mark K. Mondol, Feng Zhang and Professor Henry I. Smith

Figure 1 is a photograph of the scanning-electron-beam lithography system (VS-26) located in the scanning-electron-beam lithography (SEBL) facility, Room 38-165. This instrument was put together at MIT from two systems (VS-2A and VS-6) obtained as gifts from IBM in the mid 1990's. It has a minimum beam diameter of about 12 nm and is capable of creating large-area patterns composed of multiple stitched fields. Conversion software has been developed which allows a CAD data file to be fractured and translated prior to exposure. Substrates up to 20 cm diameter can be exposed at linewidths down to 30 nm. In order to write concentric circular patterns, such as Fresnel zone plates, software was developed to generate arbitrary arcs of an annulus with user-specified start and finish radii and angles.

The SEBL facility also houses a Raith Turnkey 150 system as shown in Figure 2. Its electron-optical column is essentially identical to that of a Gemini SEM, and provides a beam diameter as fine as 5 nm. Linewidths of 17 nm have been written with the system, as illustrated in Figure 3

The goals of the SEBL facility are to: (1) provide the MIT research community with an in-house SEBL capability for writing directly on experimental device substrates; (2) advance the state-of-the-art in SEBL, particularly with regard to pattern-placement accuracy and long-range spatial-phase coherence; and (3) pattern masks for photo, x-ray and imprint lithography.

The VS-26 and Raith 150 are heavily used in a variety of projects, both mask making and direct write. These have included: 3-D, 2-D, and 1-D photonic bandgap structures; optical-communication filters; arrays of Fresnel zone plates; electrical contacts to nanowires; high-density magnetic nanodots and rings for information storage; distributed-feedback lasers; sub-100 nm electronic devices; double-gate sub-100nm MOSFETs; diffractive optical elements; and magnetic-random-access-memory devices.

The Raith 150 is used in a program to develop spatial-phase-locked e-beam lithography. The objectives of this program are to achieve sub-1 nm pattern-placement accuracy, and to reduce the cost and complexity of SEBL. In a conventional SEBL system costing several million dollars, pattern placement accuracy is typically much worse than 10 nm.



**Figure 1.** Photograph of the VS-26 scanning-electron-beam lithography system.

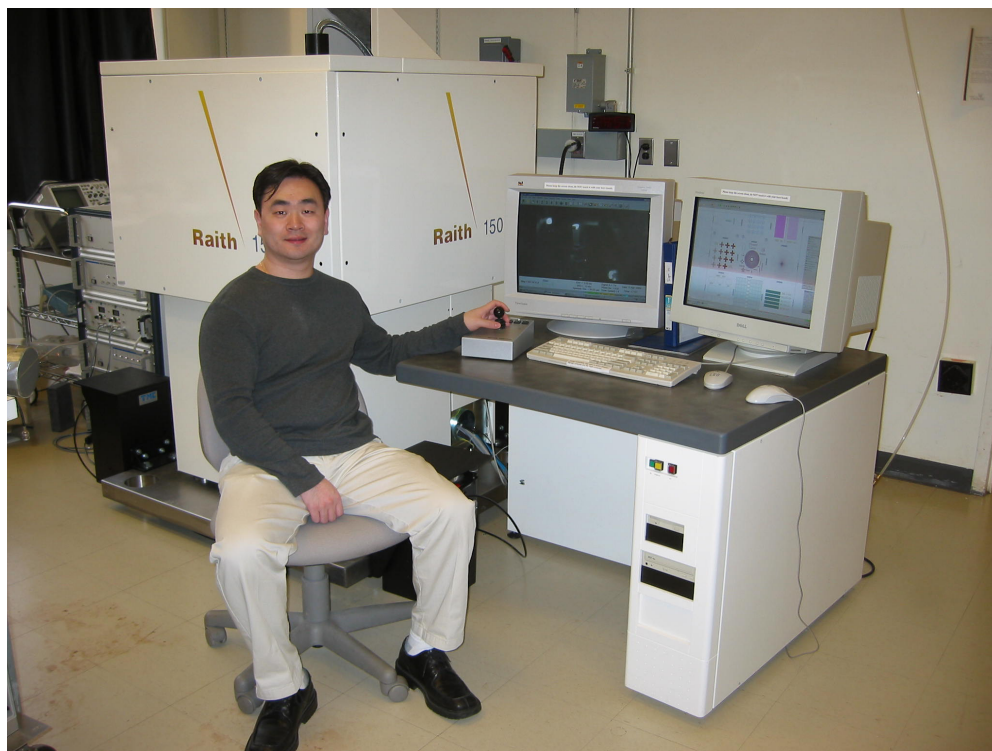


**Figure 2.** The Raith-150 electron-beam lithography system. This tool provides sub-20-nm patterning resolution, and pattern-placement accuracy  $\sim 1$  nm via spatial phase locking. The operator is graduate student Feng Zhang.

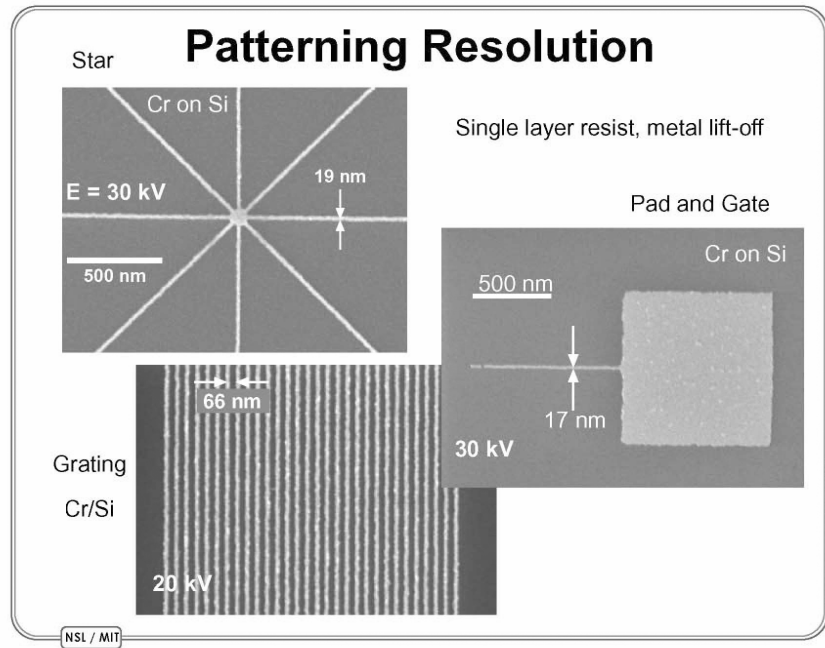


Figure 3: Scanning-electron micrograph illustrating the resolution of the Raith 150 SEBL system.

### 3. Spatial-Phase-Locked Electron-Beam Lithography

#### Sponsors:

Defense Advanced Research Projects Agency & U.S. Army Research Office  
Grant DAAD19-99-1-0280

#### Project Staff:

Cynthia Caramana, J. Todd Hastings, Mark K. Mondol, Sander Smits, Feng Zhang, and Professor Henry I. Smith

Our research in spatial-phase-locked electron-beam lithography (SPLEBL) is aimed at reducing pattern-placement errors in electron-beam-lithography systems to the 1 nm level. Such high precision is essential for a variety of future lithographic applications. SPLEBL is currently the only approach capable of achieving such accuracy. As shown in Figure 1, SPLEBL uses a periodic signal, derived from the interaction of the scanning e-beam with a fiducial grid on the substrate, to continuously track the position of the beam while patterns are being written. Any deviation of the beam from its intended location on the substrate is sensed, and corrections are fed back to the beam-control electronics to cancel errors in the beam's position. In this manner, the locations of patterns are directly registered to the fiducial grid on the substrate.

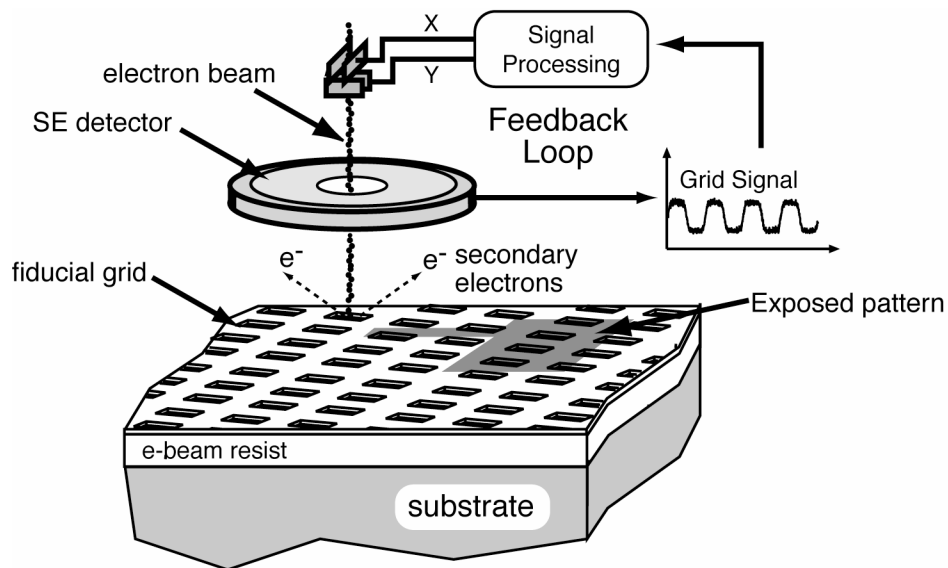


**Figure 1:** Schematic of the global-fiducial-grid mode of spatial-phase-locked electron-beam lithography. The periodic signal detected from the fiducial grid is used to measure placement error, and feed a correction signal back to the beam deflection system.

In the past, we implemented several modes of SPLEBL on a Raith150 scanning e-beam lithography system (an inexpensive system that provides sub-20-nm patterning resolution). The most attractive one among these is the continuous-feedback mode, which provides the best placement accuracy, but also is compatible with conventional scanning-electron-beam-lithography (SEBL) tools. The continuous-feedback mode allows the beam position to be constantly monitored and corrected during exposure. To do so requires that a reference grid cover the entire substrate but not perturb the electron-beam. Toward this end, we place a thin

(<10 nm) metallic fiducial grid on top of the e-beam resist. During exposure, a periodically varying secondary-electron signal is produced as a result of the interaction between the electron beam and the metal reference grid. The grid layer is essentially transparent to the primary electron-beam. Figure 2 shows interfield stitching measurements for the continuous-feedback-mode implementation.

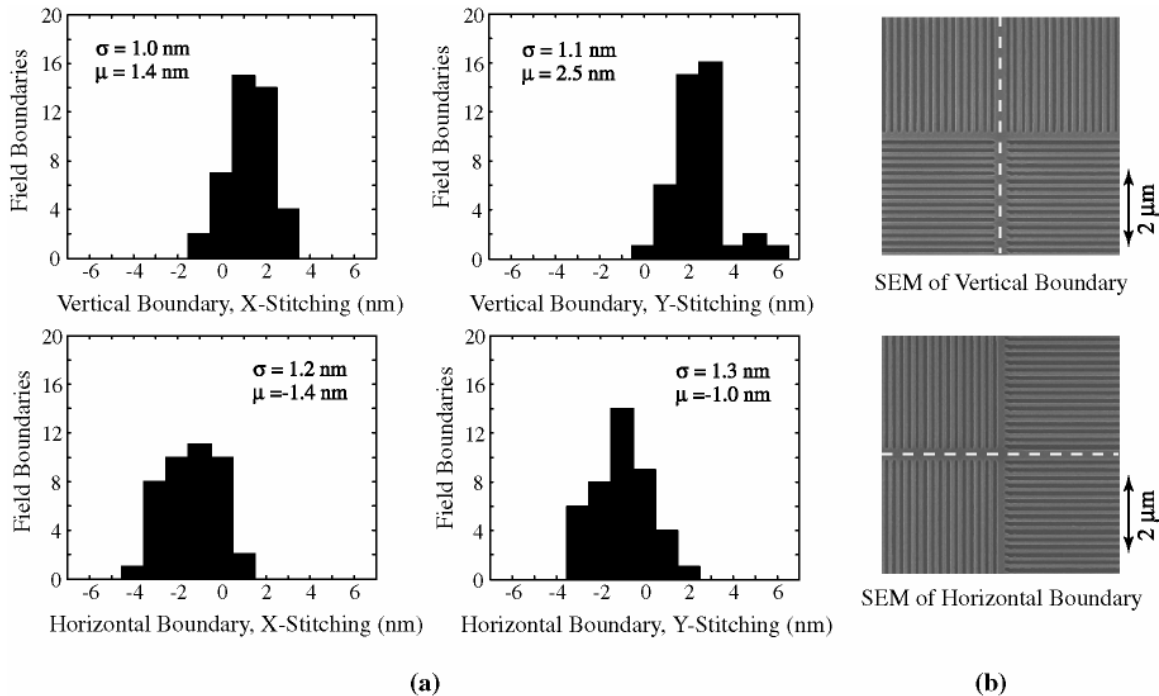


**Figure 2:** (a) Histograms showing x- and y-stitching measurements at all 84 field boundaries of 49 stitched fields. Spatial-phase locking has reduced the standard deviation of the stitching errors to below 1.3 nm. (b) Sample 200-nm period stitched grating patterns. The dashed line indicates the field boundary.

The continuous-feedback mode requires a continuous reference signal for accurate beam-position tracking. With the existing beam blanking system, the Raith150 system can only provide two states to the beam, fully-on or fully-off. As a result, accurate beam-position locking is only possible for very sparse patterns. To resolve this problem, we have developed a simple dose modulation scheme utilizing the existing beam blander. In this scheme, a much lower voltage is applied when modulating the beam during exposure. This allows a small fraction of the beam to leak through the current-limiting aperture. This slight amount of current will generate sufficient signal for continuous spatial-phase locking, yet it is insufficient to expose the resist. The scheme is currently under preliminary testing. One disadvantage of this implementation is that the beam shifts from its original position when it is partially blanked, and the shift in position needs to be tracked and taken into account in the phase-locking algorithm.

Several other dose-modulation schemes that do not shift the beam are currently under evaluation. Figure 3 shows a scheme that can modulate the beam current by altering the beam shape with an electrostatic quadrupole lens. By combining the quadrupole lens with a focusing element and a properly located aperture, one should be able to obtain the required current modulation. Because of its strong focusing, the quadrupole lens usually operates at fairly low excitation voltages. It can be adopted in extremely fast SEBL tools.

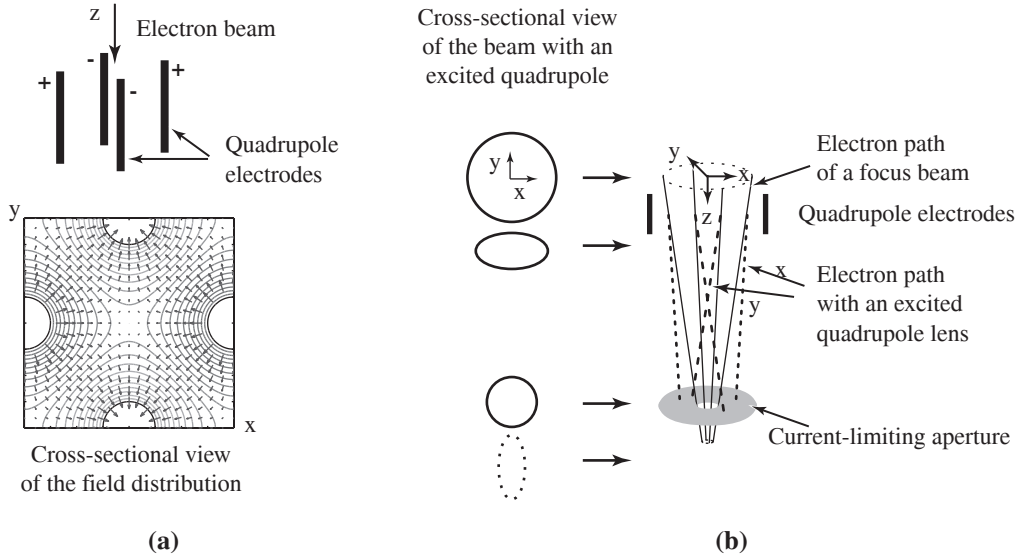


**Figure 3:** Quadrupole lens can be used as a current-modulating device. **(a)** Field distribution of an excited quadrupole lens. The e-beam will pass through the center of the field. The semi-circles represent the four electrodes of the lens. **(b)** A current modulator consists of a focusing electromagnetic lens located above the quadrupole (not shown), the quadrupole lens and an aperture located at the focal point of the electromagnetic lens. The solid lines show the electron trajectories when the quadrupole lens is not excited, and the dashed lines when the quadrupole is excited. Fairly symmetric beam shape should be obtained when proper operating conditions are met.

During the exposure, an 8-nm thick, 250-nm period Al fiducial grid placed on the e-beam resist was used to generate the reference signal necessary for spatial-phase locking. As one of the key elements in the SPLEBL technology, we believe that a non-perturbative, economical and user-friendly fabrication process for the reference grid is crucial to the success of the technology. Traditional manufacturing process requires multiple layers of thin films for photolithography and pattern transfer. It involves many spin-coating and evaporation steps, and, therefore, can be very complicated, costly, and prone to errors. A novel photosensitive dry-etching process is currently under investigation (shown in Fig. 4). In this process, a polymer film consisting of photosensitive material is spun onto the Al layer. When exposed under UV light, the photosensitive chemicals in the polymer film react with the Al underneath, and “dissolve” the Al into the polymer film. The polymer film can then be washed away with isopropanol, leaving the patterned Al film on e-beam resist.

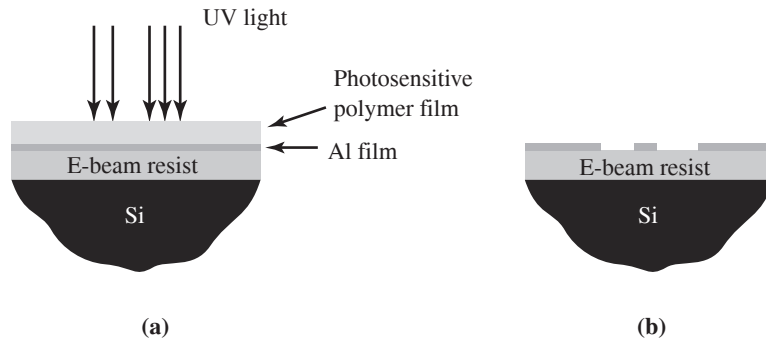


**Figure 4.** Photosensitive dry-etching process for fabricating 250-nm period Al grid on e-beam resist.

The current spatial-phase locking subsystem uses a general-purpose processor to calculate the phase error and the correction signals. The processing becomes computationally intensive as the number of samples and bandwidth increases. As the system is further optimized for throughput and affordability, the need for inexpensive, yet very fast phase locking and error-correction computation arises.

A custom hardware solution in the form of a dedicated chip is currently being developed to carry out the functions of the spatial-phase-locking subsystem. Figure 5 shows how the spatial-phase locking (SPL) subsystem is integrated with the Raith150 SEBL system. The functional block diagram of this SPL subsystem can be seen in Fig. 6. The SPL circuitry performs three major functions, phase detection, position-error calculation, and correction signal generation. Using a top-down design approach, the functional blocks are reduced to more primitive functions that are described in terms of primitive hardware functional blocks (i.e. adders, multipliers, and registers, etc.). This low-level design is converted into a hardware description language necessary for programming a field-programmable gate array (FPGA ) or generating an application-specific integrated circuit (ASIC).

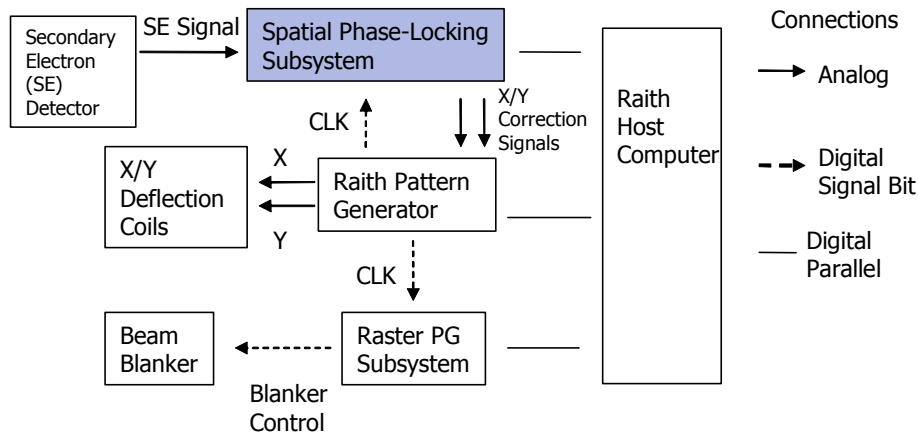


**Figure 5:** The Raith 150 SEBL system adapted for SPLEBL with the SPL subsystem highlighted.

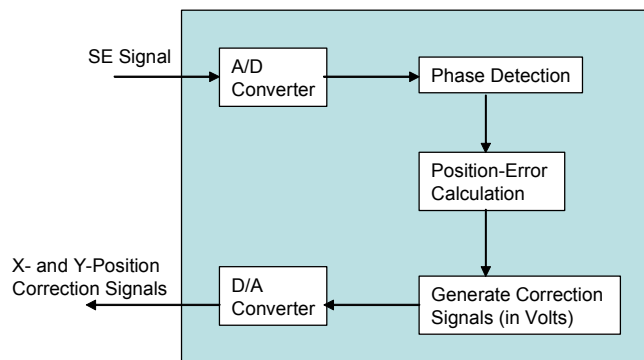


**Figure 6:** Functional block diagram of the SPL subsystem.

#### 4. X-Ray Nanolithography

**Sponsors:**

Defense Advanced Research Projects Agency and University of Wisconsin  
Contract # A720156

**Project Staff:**

Lynn Chen, James M. Daley, Euclid E. Moon, and Professor Henry I. Smith

For several years, we have been developing the tools and methods of x-ray nanolithography. We have explored the theoretical and practical limitations, and endeavored to make its various components (e.g., mask-making, resists, electroplating, sources, alignment, etc.) reliable and “user-friendly.” Because of the critical importance of x-ray mask technology, we discuss this in a separate section.

X-ray nanolithography (XNL) is a reliable and simple means of replicating patterns with feature sizes down to about 20 nm. Typically, the x-ray mask is made with scanning-electron-beam lithography (SEBL), although we often employ a combination of interference lithography, photolithography, SEBL, and XNL to fabricate the mask. Once the mask is fabricated it can be replicated repeatedly. The simplicity and process latitude of XNL make it ideally suited for certain research.

In the NanoStructures Lab (NSL), x-ray lithography has been used in the fabrication of a large variety of structures and devices, including: photonic bandgap devices, short-channel MOSFETs, and optical channel-dropping filters.

Our sources for x-ray nanolithography are simple, low-cost electron-bombardment targets. We utilize the L line of copper at  $\lambda = 1.32$  nm. The sources are separated from a helium-filled exposure chamber by a 1.5  $\mu\text{m}$ -thick  $\text{SiN}_x$  vacuum window. Figure 1 is a photograph of one of our x-ray lithography systems.

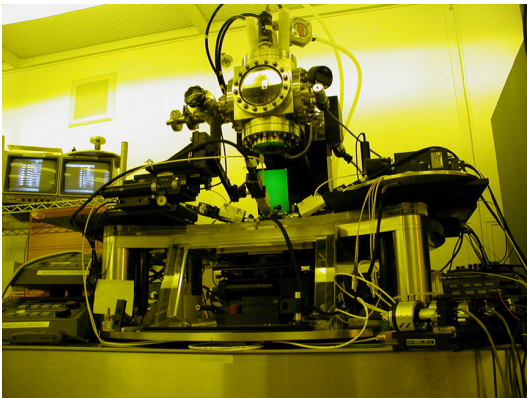


**Figure 1:** Photograph of x-ray lithography system equipped with an alignment system capable of 1nm precision.

Although the wavelength used is very short (1.32 nm) compared to the minimum feature sizes of interest (e.g., 20 nm) diffraction in the gap between the mask and the substrate can be detrimental. For example, with a  $\text{Cu}_L$  source, a 50 nm feature must be exposed at a mask-to-substrate gap of less than about 4  $\mu\text{m}$  in order to maintain good process latitude. A 25 nm feature would require a gap of 1  $\mu\text{m}$ . For such very small features, we eliminate the gap and use contact between the substrate and the flexible membrane mask. This technique has enabled us to replicate features as small as 20 nm in a practical, reproducible way as shown in Figure 2.

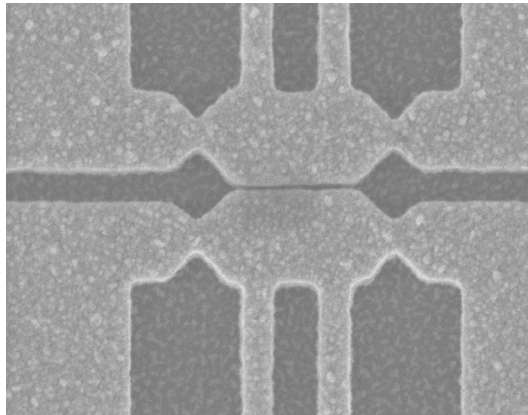


**Figure 2.** Scanning electron micrographs of device pattern with feature size ~ 20nm achieved by x-ray nanolithography.

We are currently investigating if gaps below 4  $\mu\text{m}$  can be reliably measured and controlled. For this, the substrate will have to be much flatter than 1  $\mu\text{m}$ , something that is easily achieved with an appropriate pin chuck such as those used in modern optical-projection-lithography steppers. For measuring gaps below 4  $\mu\text{m}$  we will use the “transverse chirp gapping” scheme described elsewhere in this report.

## 5. Adaptive-Membrane-Mask Technology

### **Sponsors:**

Louisiana State University, Contract R110030

### **Project Staff:**

James M. Daley, Thomas B. O'Reilly, Professor Martin Feldman (LSU), Professor George Barbastathis and Professor Henry I. Smith

Key to the mass production of submicron scale microelectronic devices is the ability to accurately transfer a master pattern to a photosensitive layer on a substrate. One factor limiting the size of the devices that can be created is the ability to transfer these patterns without distortion. Distortion can be introduced in a number of places, most significantly in the optical system used to project the pattern and in the pattern itself. The typical approach to dealing with this distortion is to create the patterns on rigid masks, and build complex and expensive optical systems to project the pattern from the mask to the substrate.

We are pursuing an alternative approach to the problem of distortion, which we call the Adaptive Membrane Mask (AMM). In this approach, the pattern is defined in an absorbing material on a thin, flexible membrane mask, typically made of Silicon Nitride or Silicon Carbide between 1 and 2 microns thick. This is the same type of mask used in x-ray lithography (XRL). Rather than trying to prevent distortion in the mask, we seek to use and control the flexibility of the mask to our advantage, with the goal of getting a better result than would be possible with even a perfectly rigid mask. In this way, our approach is akin to adaptive optics, where the shapes of flexible optical elements are controlled to correct for atmospheric turbulence. With AMM, we seek to measure and control the distortion of the mask during exposure. In the simplest form, this allows us to correct for distortion in the pattern that might have been caused by variations in the stress in the absorber. The true advantage of AMM is that it makes it possible to correct for other sources of distortion as well.

In order to control the distortion of the membrane we must first measure it. This is done with a Holographic Phase-Shifting Interferometer (HPSI), shown schematically in Figure 1. This is an interference lithography system, modified to allow it to be used to both write gratings and to read the distortion in them. First it is used to pattern a grating on the back side of the membrane mask. The pattern is then written on the front side of the mask. By putting the mask back in the HPSI, it is possible to read the distortion in the grating caused by stress in the absorber.

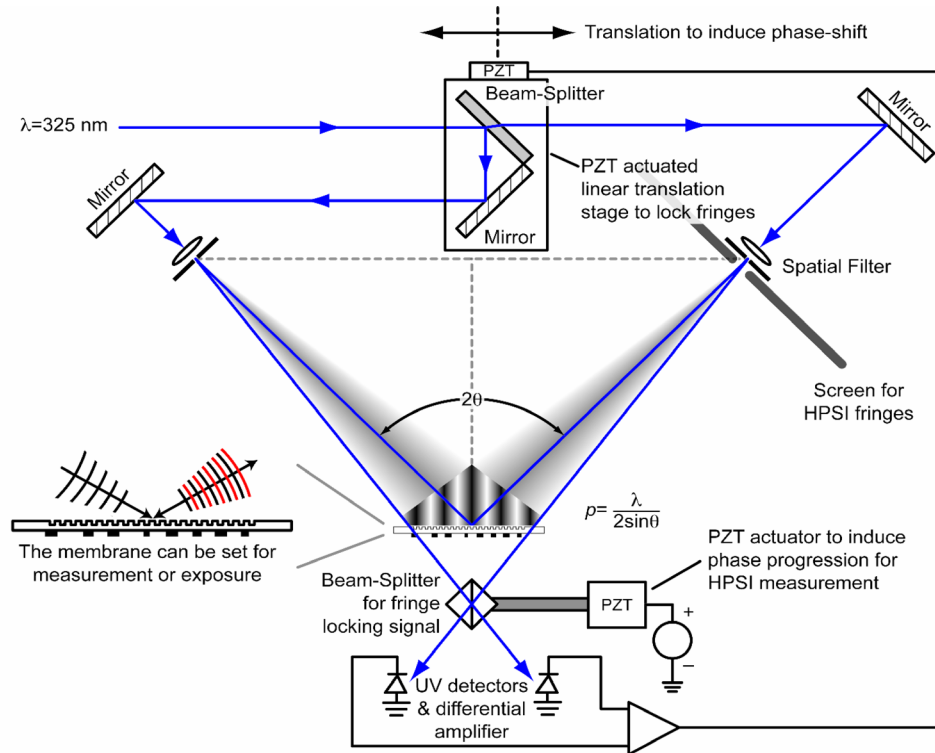


**Figure 1.** Schematic of the Holographic-Phase-Shifting Interferometer(HPSI). This setup can be used as an interference lithography system to write reference grids as well as a holographic interferometer to measure grid distortion.

A numerical method developed at MIT is then used to calculate the membrane stress required to correct the observed distortion. This stress is created in the membrane thermally, by projecting a pattern of light on the membrane to generate a desired temperature distribution across the mask. The temperature distribution can be applied to ensure that the distortion is corrected and can be adjusted iteratively if necessary. This feedback cycle can be performed in the exposure tool, by incorporating an HPSI system, or it can be done prior to exposure on a separate piece of equipment. Since distortion is directly related to membrane temperature, a thermal imaging system can be used to provide the temperature feedback needed to control temperature, and thereby distortion, during the exposure process. This second type of feedback method is illustrated in Figure 2.

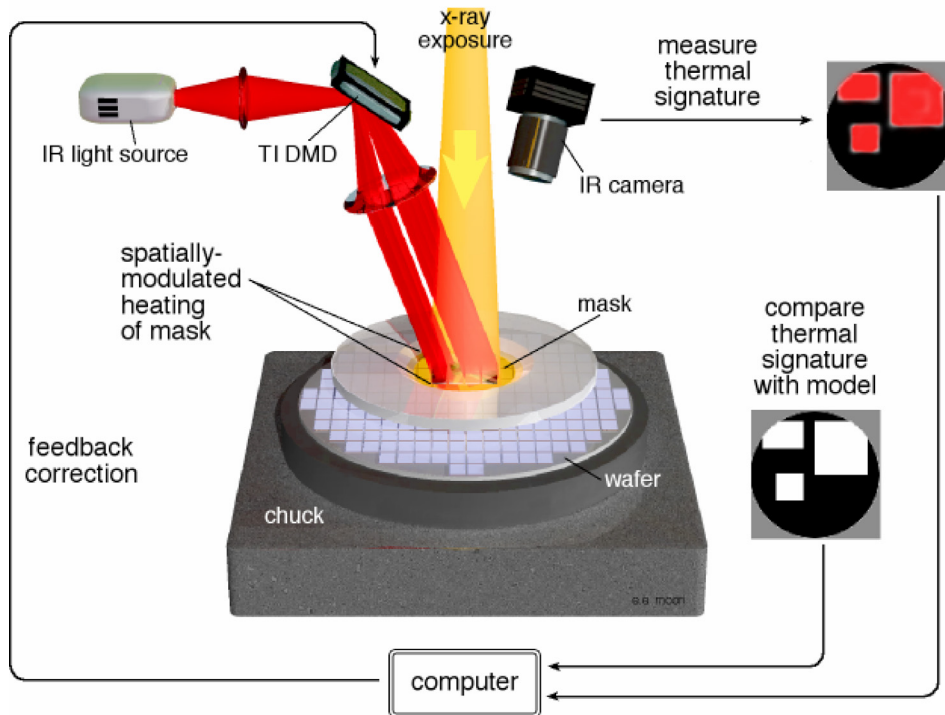


**Figure 2.** Proposed implementation of Adaptive-Membrane-Mask Distortion Correction

The adaptive membrane mask is suited for use in x-ray lithography. As membrane masks are already used in XRL, control of mask distortion is a major concern. The primary sources of distortion in XRL are stresses in the absorber layer and stress variations caused by radiation damage. XRL membrane masks used in industry are typically made from silicon carbide, which is not subject to radiation damage at exposure levels seen in industry. The ability to measure and correct distortion may allow the use of a wider range of materials for both membrane and absorber, and relax some process constraints currently needed to minimize absorber stress. For instance, masks can be made from silicon nitride, which is less expensive and easier to make than silicon carbide, but is more susceptible to radiation damage. The use of thinner membranes has the additional advantage of reducing exposure times and increasing optical transmission for mask alignment. An AMM based system can also correct for magnification errors in XRL.

To improve overlay with existing patterns on the substrate, AMM can be used to correct for distortion of the substrate, which can arise from a number of causes: high temperature processing, stress in grown overlayers, stress due to ion implantation, etc. As long as these distortions are measurable and repeatable, an adaptive mask can compensate for them, allowing more flexibility in wafer processing. For example, high temperature processes that induce wafer distortion can be used, since the AMM can compensate for them.

The advantages described above also apply to the use of AMM with other types of lithography that use membrane or stencil masks, including electron-, ion- and neutral-atom lithography. In addition, we believe that adaptive masks may be applicable to optical-projection lithography (OPL), by far the dominant technique for fabricating semiconductor chips. Although rigid masks are currently used in OPL, reducing the importance of distortion in the mask, OPL is subject to all of the other types of distortion described above, as well as aberrations in the optical system. An

adaptive membrane system may be able to correct for distortion in optical projection systems, potentially allowing the specifications of those systems to be relaxed, reducing their cost and complexity

Preliminary work has shown good agreement between experiment results and computer models. Figure 3 compares experimental and analytical results for a temperature distribution that was intended to move a square area in the middle of the membrane without distorting it. Here, displacements are plotted along a horizontal line in the middle of the membrane.

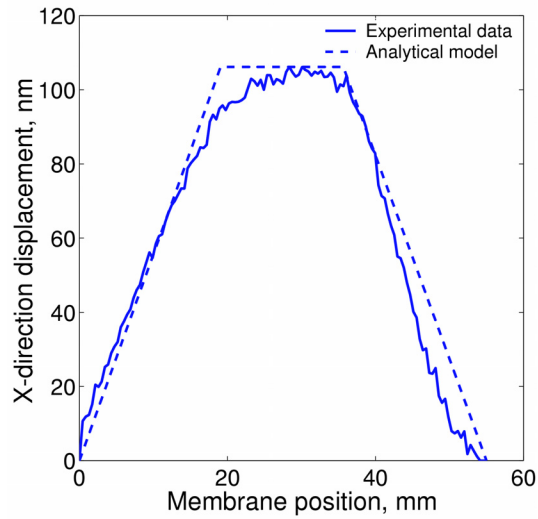


**Figure 3.** Comparison of experimental and analytical results

## 6. Nanometer-Level Feedback-Stabilized Interferometric Aligning and Gapping

### Sponsors:

JMAR/SAL Incorporated, and University of Wisconsin, Contract # A720156

### Project Staff:

Euclid E. Moon, Dr. Patrick N. Everett, and Professor Henry I. Smith

A novel aligning and gapping technique called Interferometric-Spatial-Phase Imaging (ISPI) was implemented on an in-house, custom test-bed apparatus. ISPI combines high sensitivity to alignment ( $<1$  nm) with immunity to spurious influences, such as resist or other coatings on the substrate. In ISPI, periodic structures are illuminated with oblique-incidence spatially-coherent light, forming interference patterns that are imaged by low-NA microscopes at the Littrow angle. Since the illumination and viewing paths are at an oblique angle, exposure and position correction can proceed simultaneously, eliminating errors typically associated with mechanical drift. The validity of the ISPI alignment was indicated by overlay of device structures and moiré fringes in resist (Fig. 1). The moiré fringes (Fig. 1(b,c)) are produced by overlay of two different grating periods:  $p_1/p_2$ ,  $p_2/p_1$ , and  $p_1/p_2$ , one in exposed resist, and the other etched into the substrate. The middle ( $p_2/p_1$ ) fringe set moves in the opposite direction of the surrounding ( $p_1/p_2$ ) fringes, for enhanced sensitivity. Alignment is encoded in the spatial phase relation between fringe sets, whether in the interference fringes observed by ISPI microscopes or in moiré fringes in exposed resist.

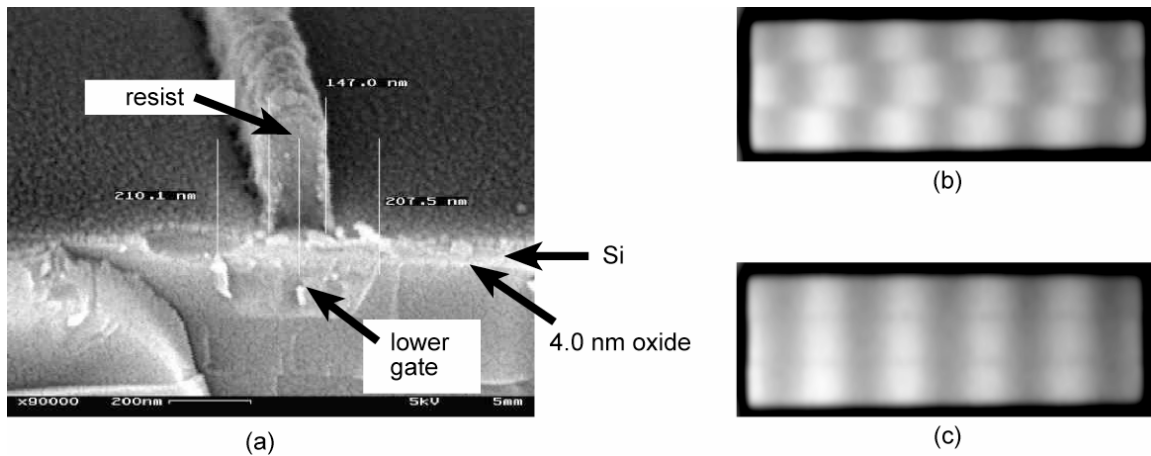


**Figure 1:** (a) SEM micrograph of gate line in resist overlaid on top of a lower gate in a double-gate FET structure. Alignment is measured to be  $<5$  nm. (b) Optical micrograph of moiré pattern between gratings etched into the substrate and exposed in the resist. Spatial phase disparity between fringe patterns indicates misalignment. (c) Aligned exposure. Overlay was measured to be 2.7 nm, including errors from source axis misalignment, e-beam writing errors, and other system errors.

In addition to overlay, highly sensitive detection of small gaps is increasingly critical for nanopositioning and proximity lithographies. In ISPI, gap is measured by a variety of means. Coarse gap is determined by the geometric separation between beams backdiffracted from a narrow grating on the mask at the Littrow angle, and the reflection of the symmetric forward diffraction off the substrate. This type of coarse gapping works over a wide range, from 300 to 30 micron gaps. Due to the large focal depth of the low-NA microscopes, refocusing on the mask

and substrate is not required. Below 30 microns, the two diffracted beams overlap, interfere, and produce intensity oscillations. Absolute gap is found from monitoring intensity oscillations during three short-range scans of gap, each with a different illumination wavelength. However, to find the gap without scanning, which is essential for feedback control, we produce interference fringes analogous to the aligning fringes by means of a checkerboard pattern on the mask, with a varying period in one direction (Fig. 2). In these marks, the gap is encoded in the spatial phase and frequency of the interference fringes. We call this gapping method Transverse Chirp Gapping (TCG). TCG operates over a range of gaps between  $<1$  and  $>30$  microns, and is sensitive to  $<10$  nm. TCG can be calibrated to the absolute gap with the previously mentioned intensity oscillations.

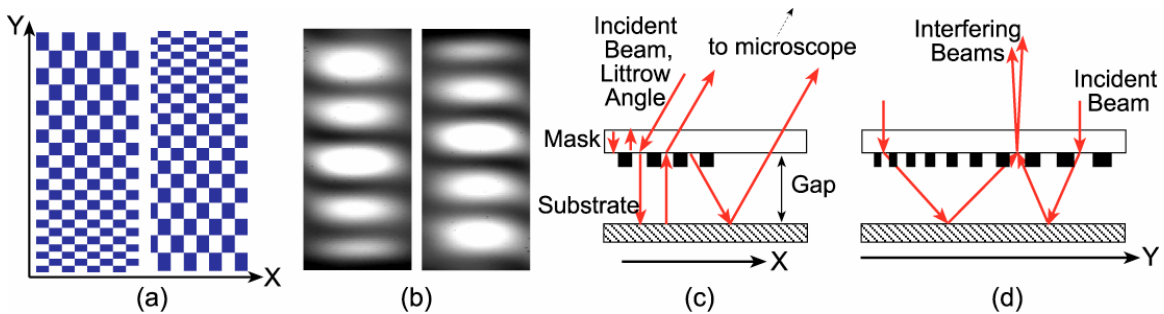


**Figure 2:** (a) Schematic of the Transverse Chirp Gapping marks. Opposite chirps in the Y direction cause the interference fringes (b) to move in opposite directions for a displacement in Z. The gap is encoded in the spatial phase and frequency of the interference fringes. (c) Schematic of diffracted beams in the X-Z plane, and light returning to the microscope at the Littrow angle. (d) Schematic of one set of diffracted beams in the Y-Z plane. A bright fringe corresponds to constructive interference from two diffracted and reflected beams. Conditions for constructive interference occur at only a few positions along the chirp. As the gap decreases, the path lengths between the mask and substrate decrease, hence the points of constructive interference and fringe spacing increase along the Y direction.

A final verification of absolute gap is found from gap-dependent frequency-multiplication in the optical field propagation beyond a periodic structure, the so-called Fractional-Talbot effect (FTE).

Absolute gap is determined by the spatial frequency content of each region in a single exposure, which varies depending on the gap and grating period,  $p$ . Gap resolution is increased beyond the lowest-order Talbot-frequency multiplication distance  $T_D = p^2/(2\lambda)$  by analysis of the frequency content of several gratings of different periods. Absolute gap with sub-10 nm sensitivity is found by matching the frequency spectra of the exposed features to fractional-Talbot simulations (Fig. 3). The FTE gap measurement confirms the calibrated TCG gap measurement.

ISPI is a general, six-axis positioning ( $X, Y, Z, \theta_x, \theta_y, \theta_z$ ) scheme that meets the requirements of any form of proximity lithography, including imprint, x-ray, ZPAL, LEEPL, proximity ion, neutral atom, or near-field photo. Some novel aspects are the utilization of spatial phase to encode position in all six axes, allowing simultaneous detection of gap and alignment in the same microscope image, derivation of rotation angles from three ISPI microscopes, and nanometer overlay of exposed features. The unique capabilities of ISPI aligning and gapping are engaged in the fabrication of a variety of electronic and optical devices.

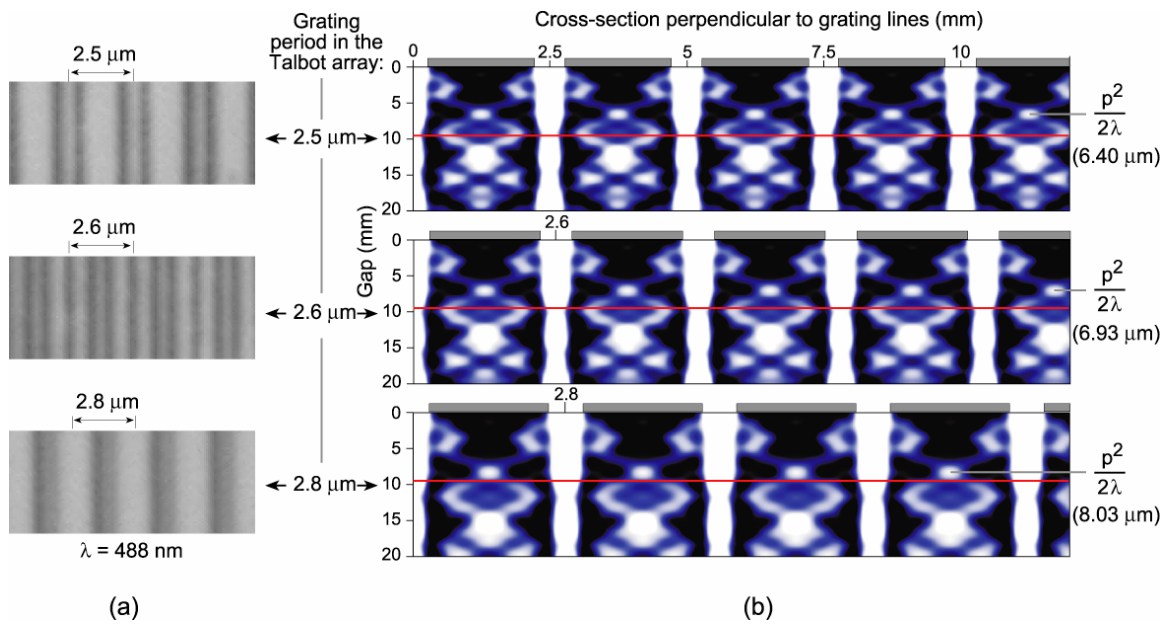


**Figure 3:** Demonstration of the Fractional-Talbot effect. (a) Three examples of spatial frequency variations from different grating periods, exposed in resist at a single, fixed gap set by TCG. (b) Simulations of intensity distribution from gratings matching the exposed grating period. The line drawn across all three simulations indicates the exposure gap. Absolute gap is determined by the spatial frequency content of each exposed region, which depends on the gap and grating period,  $p$ .

## 7. Zone-Plate-Array Lithography (ZPAL): The System

### Sponsors:

Defense Advanced Research Projects Agency and Army Research Office  
Grant No. DAAD19-01-1-0330

### Project Staff:

Rajesh Menon, Amil Patel, David Chao and Professor Henry I. Smith

Nanolithography is the key technology driving technological progress in electronics, photonics, information technology and biotechnology. However, creating large-area nano-patterns (on the order of square centimeters) is often very expensive. The tools and techniques used in the semiconductor industry have become too expensive for applications other than high-volume manufacturing. Masks, which are required for each unique design, can cost hundreds of thousands of dollars per layer. This economic constraint has made nano-patterning accessible to a select few, namely the major companies of the semiconductor industry, who can absorb these costs with high volume production. Empowering the next generation of innovators will require making available, an inexpensive yet highly capable nanolithography tool.

At the MIT NanoStructures Laboratory, we are pursuing an innovative scheme, which we call, Zone-Plate-Array Lithography (ZPAL). It is our vision to make robust nano-patterning a pervasive technology. ZPAL's emergence and feasibility is made possible by improvements in computation power, planar lithographic technologies and micromechanics. ZPAL is an optical maskless technology that operates on the principle of diffraction rather than refraction. This means we can supplant the expensive masks and complex optical systems that characterize traditional semiconductor lithography tools. In this maskless model there is minimal marginal cost for realizing new designs, encouraging engineers and scientists to take risks on new designs.

Instead of a single, massive lens, an array of hundreds or thousands of microfabricated Fresnel-zone-plate lenses is used, each focusing a beam of light onto the substrate. A computer-controlled array of micromechanical mirrors turns the light to each lens on or off as the stage is scanned under the array, thereby printing the desired pattern in a "dot-matrix" fashion. A schematic of ZPAL is shown in Figure 1.

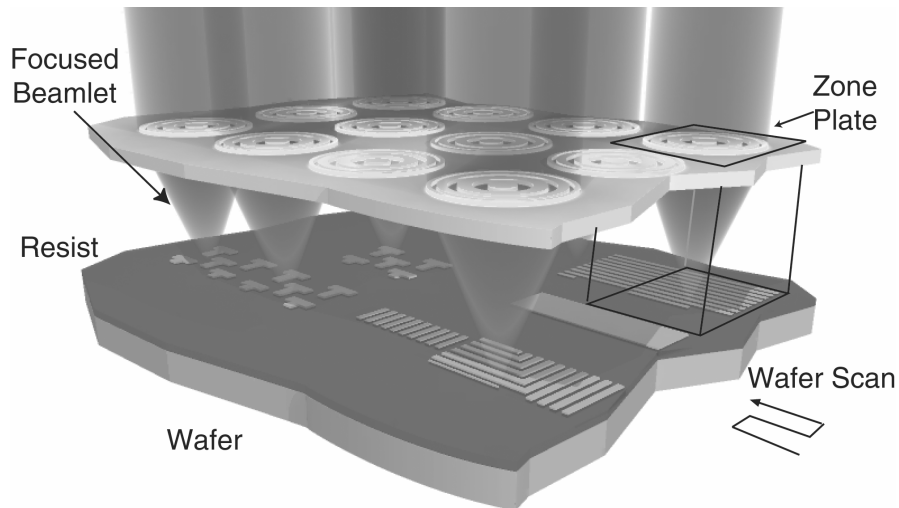


**Figure 1:** Schematic of zone-plate-array lithography (ZPAL). An array of Fresnel zone plates focuses radiation beamlets onto a substrate. The individual beamlets are turned on and off by upstream micromechanics as the substrate is scanned under the array. In this way, patterns of arbitrary geometry can be created in a dot-matrix fashion. The minimum linewidth is equal to the minimum width of the outermost zone of the zone plates.

Past research achievements include the development of a ZPAL test-bed which has proven the lithographic performance of zone-plates. This experimental success included the fabrication of zone-plate-arrays (Figure 2) and the development of simulation tools. Current research builds upon these achievements to come closer to a functional prototype. Here, the progress of the micromechanics and lithography results using proximity-effect correction are discussed.

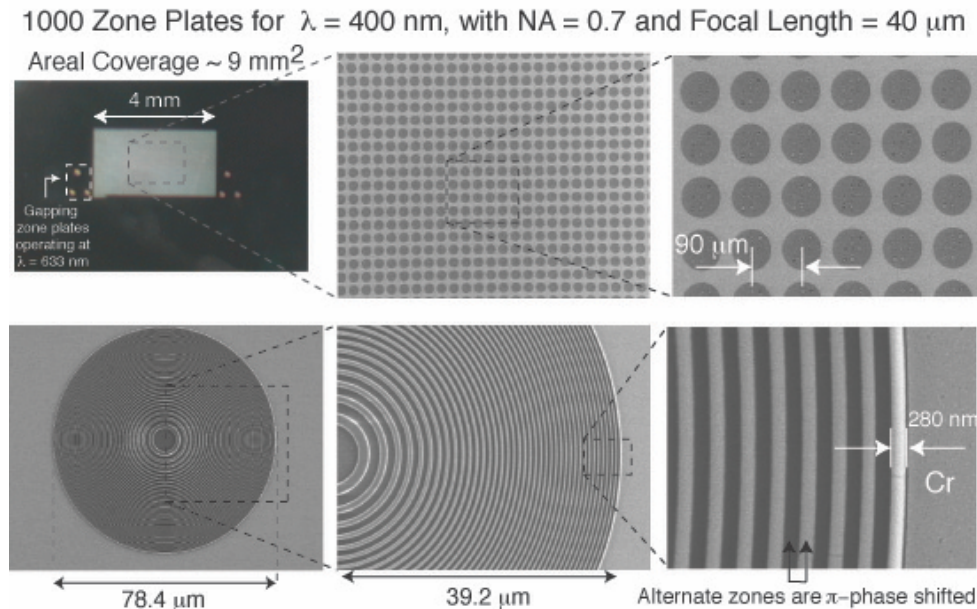


**Figure 2:** Large zone plate arrays can be readily fabricated with our novel process that requires a single lithography exposure and no etching, even for the case of phase zone plates. Top-left: Optical micrograph showing an array containing over 1,000 zone plates with an areal coverage of  $9 \text{ mm}^2$ . Bottom-right: Detail of the outer-most zones. The duty-cycle is very close to 50%, and the phase shift between alternate zones ( $180^\circ$ ) was controlled to about 1%.

### Integration of Micromechanics

We have selected the Grating Light Valve (GLV<sup>TM</sup>) technology manufactured by Silicon Light Machines, as the spatial light modulator for the zone-plates (Figure 3). The GLV micromechanics consist of a linear array of 1088 elements which can achieve 256 gray levels (8-bits) and can switch at frequencies well over 1 MHz. The individual elements modulate light using the principle of diffraction, which will potentially allow us to operate at short wavelengths, probably down to 157nm. These attributes make this device highly suitable to the ZPAL architecture. Current research focuses on linking the GLV to the ZPAL test-bed electronically (data input and control) and optically.

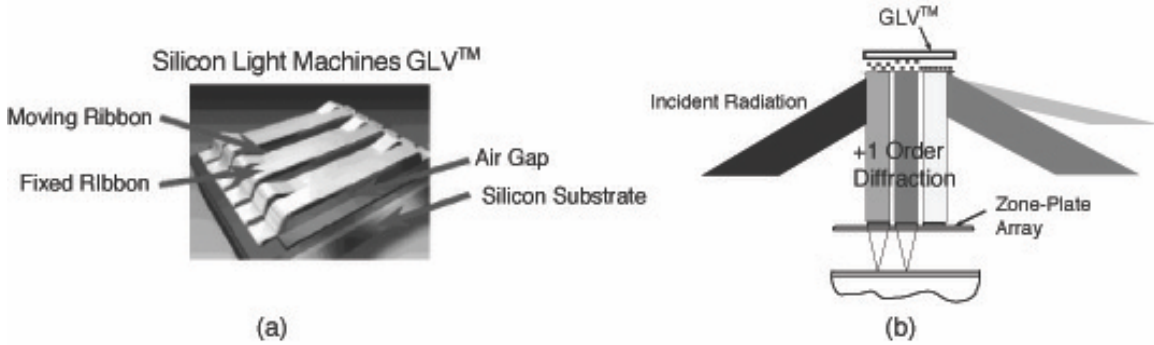


**Figure 3:** Schematics of the Silicon Light Machines Grating Light Valve (GLV) device. (a): A single element showing fixed and electrostatically-deflected moving ribbons creates a variable-height grating. (b): Incident light will be diffracted from the grating at a known angle, with varying intensity depending on the height of the grating. Each pixel, a small patch of the grating, diffracts onto a single zone plate, depth turning on and off (or grayscale) each pixel written onto the substrate in ZPAL.

The GLV device is stand-alone. A data-delivery infrastructure was independently developed to maximize the tradeoffs between cost, flexibility, performance and design time, programmable hardware developed by National Instruments was selected for the data-delivery system. In the past, it was demonstrated that the system could send frames of data to the GLV with a maximum throughput of nearly 1Gbit/s. Recently, we have developed the software architecture that bridges a 2-D pattern created by the user with the GLV hardware. Using a combination of real-time and offline processing to circumvent bottlenecks, a sustained throughput of nearly 250 MBit/s was demonstrated. In addition, control logic was developed to synchronize the flow of data to the GLV with the stage motion.

After developing the data-delivery system, the next challenge became designing projection optics that relay the light from the GLV onto the zone-plate array. Initial results with the multiplexing capability are shown Figure 4. These results demonstrate proper functionality of the data-delivery and control hardware.

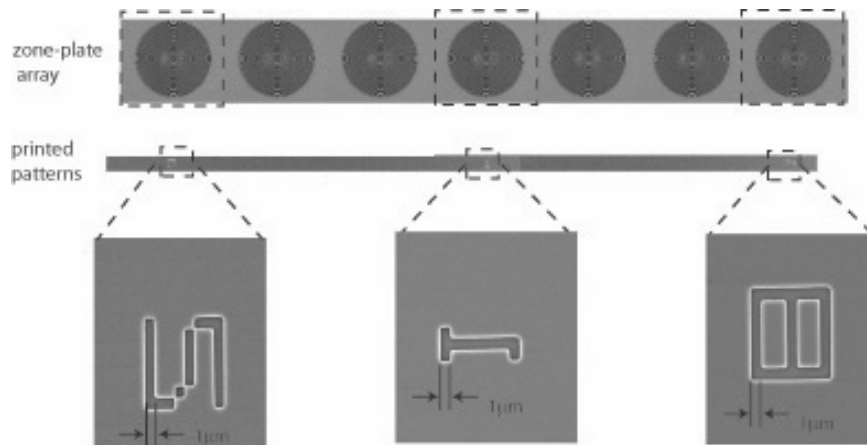


**Figure 4:** Parallel patterning with ZPAL. Top: Scanning-electron micrograph of a linear zone-plate-array (ZPA). Middle: Scanning-electron micrograph of patterns printed in resist using the above ZPA. Bottom: Magnified scanning-electron micrographs of the printed patterns. Note that data was sent to the GLV such that one zone plate out of every 3 was writing, and different zone plates wrote different patterns simultaneously.

## 8. Zone-Plate-Array Lithography (ZPAL): Pushing Lithographic Performance

### Sponsors:

Defense Advanced Research Projects Agency and Army Research Office  
Grant No. DAAD19-01-1-0330

### Project Staff:

Rajesh Menon, Amil Patel, David Chao, and Professor Henry I. Smith

In a direct-write system such as ZPAL, the major lithographic figures-of-merit are resolution and contrast. Resolution is quantified by the following equation:

$$W_{\min} = k_1 \lambda / NA, \quad (1)$$

where  $W_{\min}$  is the minimum feature size, NA is the numerical aperture of the zone plate,  $\lambda$  is the exposure wavelength, and  $k_1$  is a proportionality factor that, in effect, indicates how close to theoretical limits one operates.

The ZPAL results presented in Figure 1, using NA=0.9, illustrate high fidelity, small edge roughness, and the patterning of dense features down to the minimum spot size.

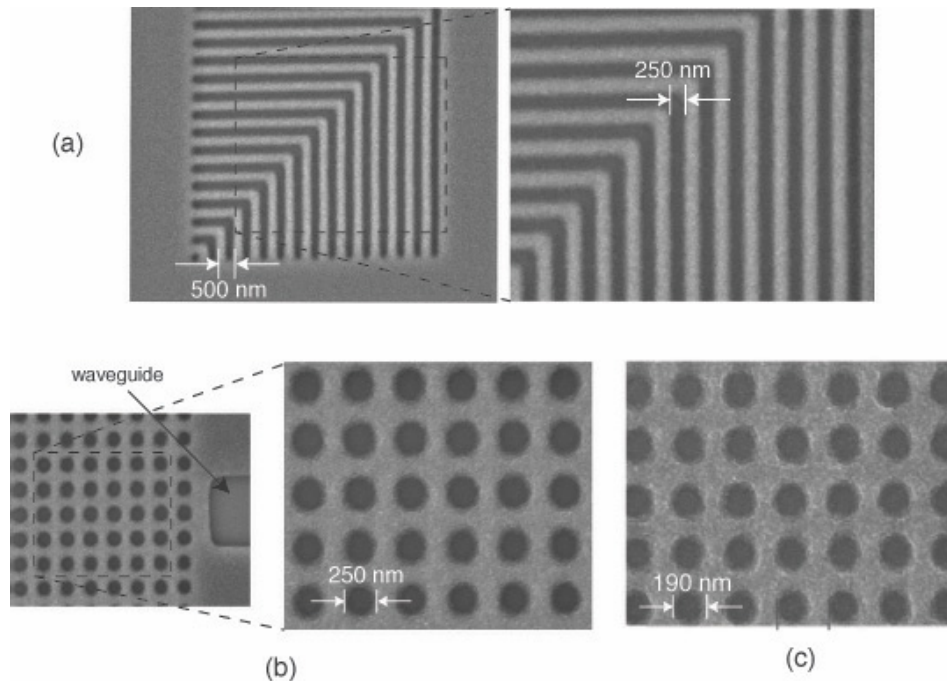


**Figure 1:** Scanning electron micrographs of patterns exposed with our continuous-scan 0.9 NA ZPAL system operating at  $\lambda = 400\text{nm}$ . (a) Dense nested Ls, (b) 2D photonic-bandgap structures with 500 nm period, (c) 2D photonic-bandgap structures with 360 nm period.

The minimum feature size can be further reduced by decreasing  $k_1$ . This corresponds to decreasing the size of the address grid, as illustrated in Figure 3. The limit to which  $k_1$  can be reduced, is determined mainly by the contrast of the photoresist.

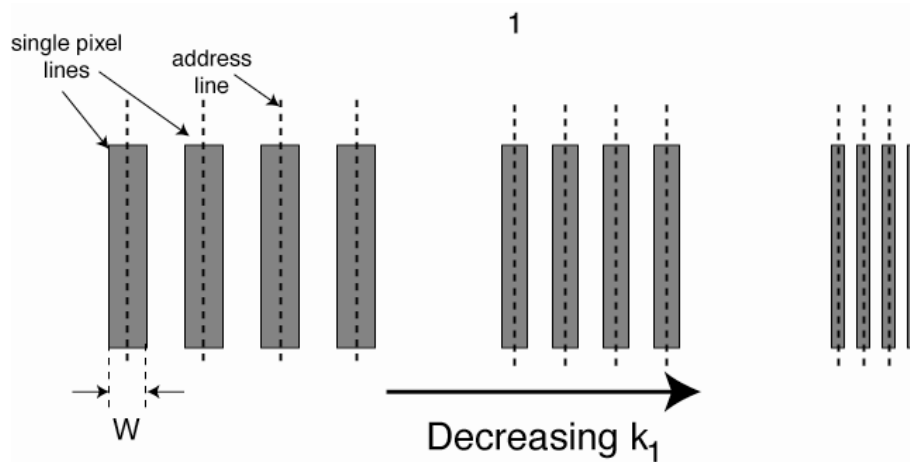


**Figure 2:**  $k_1$  in ZPAL. Decreasing  $k_1$  decreases the minimum feature size. This is done by decreasing the address grid of the system i.e. the scan lines of the focused spot are brought closer together as shown. At some point, the final image will not have sufficient contrast to be resolved by the photoresist. That point determines the limiting  $k_1$  factor.

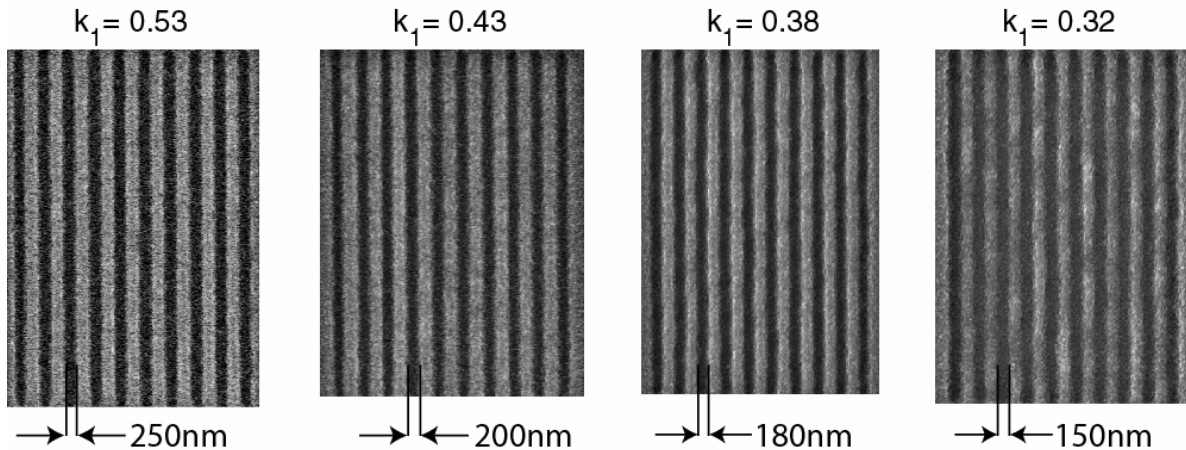


**Figure 3:** Exploring the limits of  $k_1$  with ZPAL. High-numerical-aperture zone plates (0.85 and 0.9) can operate at low  $k_1$  factors (below 0.4). Sub-60 nm patterning should be possible, by operating at the demonstrated  $k_1=0.32$ , with 0.9NA zone plates and  $\lambda = 157\text{nm}$ .

Figure 3 shows a set of scanning-electron micrographs of dense lines and spaces with varying  $k_1$ 's, from 0.53 to 0.32. Systematic characterization of lithographic exposures indicated that the process latitude for our current system is more than 10% (even when operating at  $k_1 = 0.32$ ).

Reducing  $\lambda$  below 400 nm is difficult due to the high cost and limited number of CW sources. A cost effective solution is to reduce the *effective wavelength* of the exposing radiation using water immersion lithography. In the basic immersion scheme, the gap between the last optic (the zone plates in our system) and the substrate is filled with water. This effectively decreases the

operating wavelength by a factor of  $n_i$ , where  $n_i$  is the index of refraction of the immersing liquid. Continuing with water as the example ( $n_i=1.35$ ), we can expect a 26% decrease in the feature size using this scheme. Our setup is depicted in Figure 4.

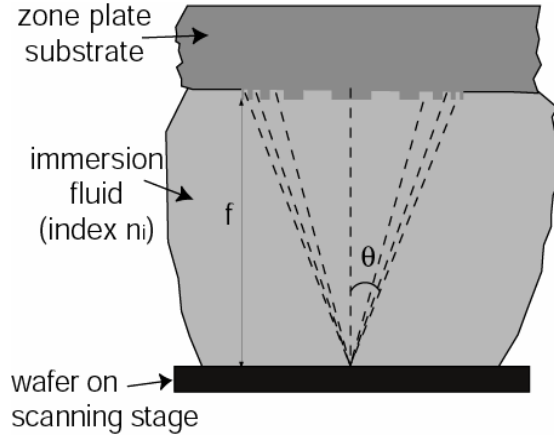


**Figure 4:** Immersion Lithography for ZPAL. We place a droplet of immersion liquid (e.g. water) on the substrate, then lower the zone plate array face down making contact with the immersion liquid.

There are many challenges to incorporating immersion lithography into the existing ZPAL system. Fabricating zone plates suitable for immersion lithography in our system is the first obstacle. We have previously shown a robust planar process, involving HSQ resist and a fused silica substrate, to fabricate zone plates for the non-immersion scheme. The proper functionality of a zone plate is dependent upon introducing a half wavelength phase shift between adjacent zones. This phase shift becomes difficult when the indices of refraction of the two materials, HSQ and water (the immersing liquid), are nearly identical. In such a case, the zone plates would need to be  $2\mu\text{m}$  thick. The required aspect ratio of 10:1 (feature thickness to feature width) is difficult to obtain with the old process.

We are currently investigating two different zone plate designs for immersion. Schematics of both are shown in Figure 5. The first design requires the patterning of HSQ zone plates on a  $1\mu\text{m}$ -thick SiN membrane. The flatness and fragility of the membrane is the primary concern, but being able to adapt much of the old zone-plate fabrication process is an advantage. The second design (the more durable and robust solution) will be to etch the zone plates into a sapphire substrate and then fill the zones with HSQ resist to create a high refractive index difference as well as to provide a protective coat. This design, while more difficult to process, will be more reliable in the long run.

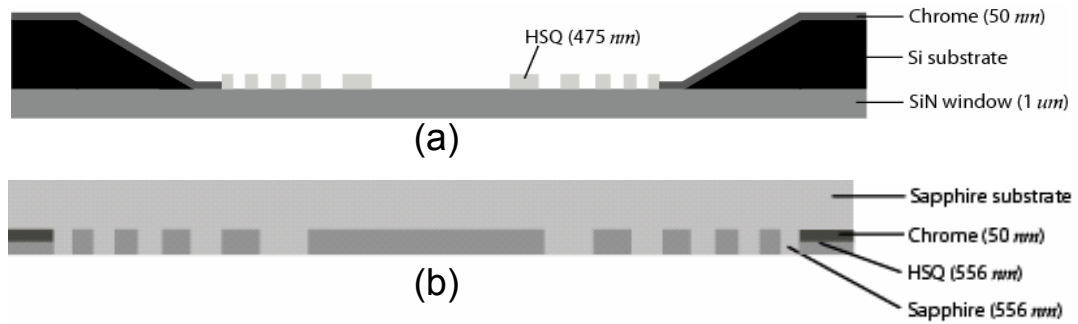


**Figure 5:** Two zone plate designs for immersion lithography. (a) HSQ zone plates defined in a SiN membrane, (b) zone plates etched in sapphire substrate, then filled with HSQ.

The successful implementation of the immersion scheme for ZPAL will extend the resolution of our ZPAL system to below 100 nm.

Image contrast is a second important lithographic figure-of-merit. This is particularly important because phase zone plates have higher (odd) diffraction orders, which contribute to the background around the focused spot. We have shown that large area patterning is indeed possible with zone plates, even without order-sorting apertures, and at very high numerical apertures.

For evaluating contrast, it is sufficient to pattern full fields at the maximum resolution. Figure 6 demonstrates that full fields of dense lines and spaces can be written with high-NA zone plates. The figure contains an experimental result in which we exposed fields of  $125\mu\text{m} \times 125\mu\text{m}$  (currently the scanning limit of our stage) with 0.85 NA zone plates operating at  $\lambda=400\text{nm}$  and focal length of  $40\mu\text{m}$ . A field of  $125\mu\text{m} \times 125\mu\text{m}$  corresponds to the area under a 0.85 NA zone plate, as indicated in the figure. The exposed pattern consists of 1:1 dense lines and spaces with a period of  $440\text{nm}$ . The magnified scanning-electron micrograph at the bottom-right of figure 6 provides a clear view of what the pattern looks like, namely a  $440\text{nm}$ -period dense 1:1 grating.

In summary, our results prove that high-numerical-aperture zone plates are capable of providing sufficient contrast for state-of-the-art lithography. Although multiple diffracted orders exist, the background exposure that they produce is not deleterious. Moreover, the background can be further reduced by the utilization of order-sorting apertures.

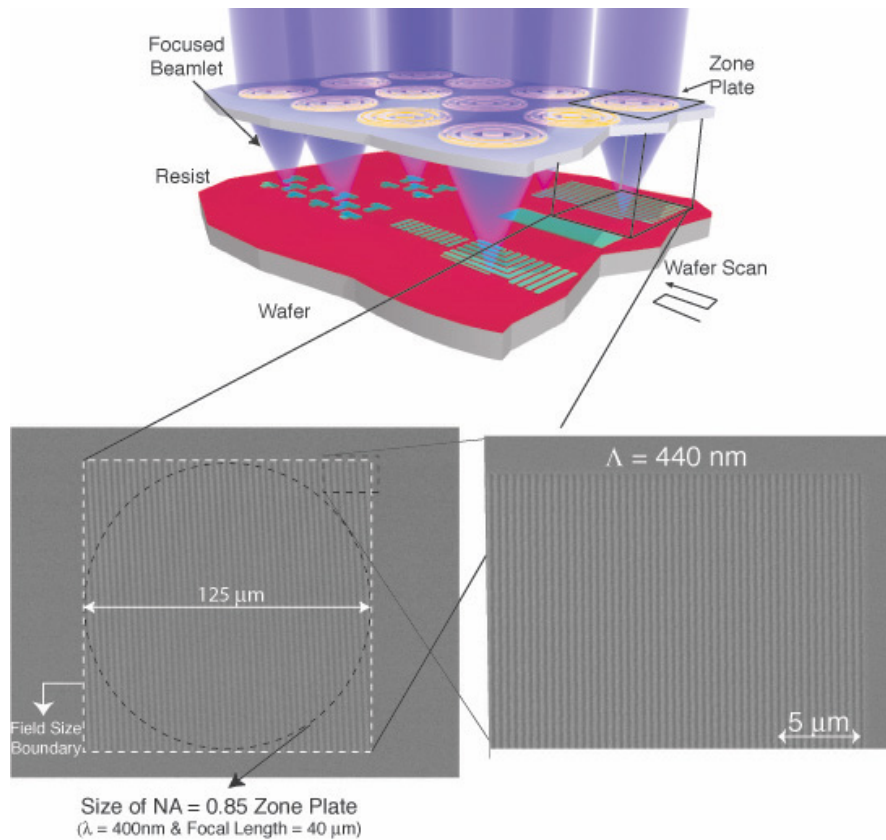


**Figure 6:** Top: Schematic of the ZPAL system without the micromechanics. Large-area patterns are created by stitching adjacent fields, with a field defined as the square area located underneath any given zone plate. Bottom-left: Proof that full-field patterning is possible with ZPAL despite the existence of multiple orders. A

dense 1:1, 440nm-period grating was exposed (with 400nm wavelength) covering the area of a 0.85 NA zone plate. Note that the inclined periodicity ( $\sim 3\mu\text{m}$  period) observed in the left scanning-electron micrograph is the result of a moiré effect (resulting from the beating of the periodic sampling of the SEM with which the picture was acquired and the periodicity of the exposed grating). Bottom-right: Zoomed in SEM of the top-right corner of the large area grating.

**Proximity Effect Correction:**

We have developed simulation tools to design zone plates as well as other diffractive-focusing elements, and to study the effect of various system parameters on the lithographic performance of ZPAL. Specifically, we have modeled the point-spread function (PSF), which is the intensity profile for the radiation at the focal plane of the zone-plate. There is good agreement between the model and the experimental performance of the zone-plates (Figure 7).

As seen in the plot of the PSF of the zone-plates, the radiation intensity of the focused spot has sidelobes. This means that during exposure, for any given pixel on the substrate surface, the total dose received must include the accumulation of background radiation from neighboring pixel exposures. If the amount of background at any given pixel-location is accurately known (a function of the pattern and the PSF) then the intensity of each pixel in the given region can be independently modulated (GLV allows for 256 levels) such that the correct pattern is produced. This process of reverse engineering a pattern is formally known as proximity effect correction (PEC).

A novel algorithm for PEC, which is computationally efficient, was developed at the NSL for use with ZPAL and potentially other direct-write tools. The efficacy is shown in Figure 8 where the same pattern is exposed with and without PEC. The difference is particularly evident in the control over the minimum feature size and the sharp corners of the shapes.

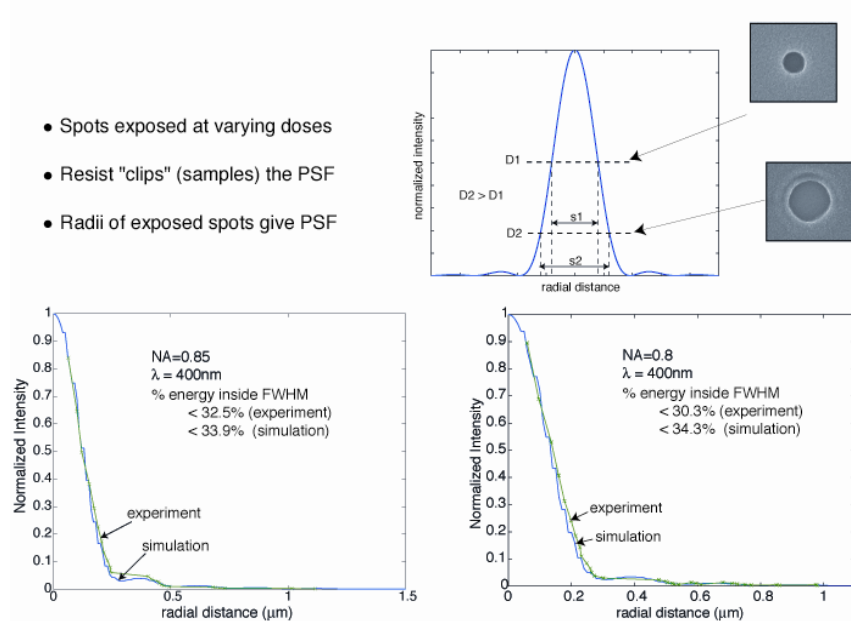


**Figure 7:** Top: Experimental process for quantifying the PSF. Spots of several exposure times were patterned in photoresist, which acts as a sampler of the PSF. The radii of the exposed spots can be assembled to form the PSF. Bottom: PSFs for zone plates of  $\text{NA}=0.85$  (left) and  $\text{NA}=0.8$ (right) were determined experimentally using the simulation tools. The results show excellent agreement.



## 9. Interference Lithography

### Sponsors:

Defense Advanced Research Projects Agency and U.S. Army Research Office –  
Grant DAAD19-99-1-0280

### Project Staff:

James M. Carter, Robert C. Fleming, Timothy A. Savas, Michael E. Walsh, Thomas B. O'Reilly,  
Dr. Mark L. Schattenburg, and Professor Henry I. Smith

Interference lithography (IL) is the preferred method for fabricating periodic and quasi-periodic patterns that must be spatially coherent over large areas. IL is a conceptually simple process where two coherent beams interfere to produce a standing wave, which can be recorded in a photoresist. The spatial-period  $P$  of the grating that can be as low as half the wavelength of the interfering light ( $\lambda$ ), allowing for structures on the order of 100nm from UV wavelengths, and features as small as 30-40 nm are possible using a DUV ArF laser. One can think of the high-contrast sinusoidal intensity images, i.e. spatial frequencies, produced with this technique as the building blocks from which more complex images are formed. Thus, one can study the process of lithography using the gratings formed with IL just as one would study an electronic or acoustical system using sinusoids rather than arbitrary signals. The periodicity of gratings produced by IL is given by

$$P = \frac{\lambda}{2\sin(\theta)}$$

where  $\theta$  is half the angle of beam intersection.

The NanoStructures Lab has been developing IL technology for about 30 years. We currently operate 4 different IL systems for a wide variety of applications. One system, shown schematically in Figure 1, is operated in cooperation with the Space Nanotechnology Lab.

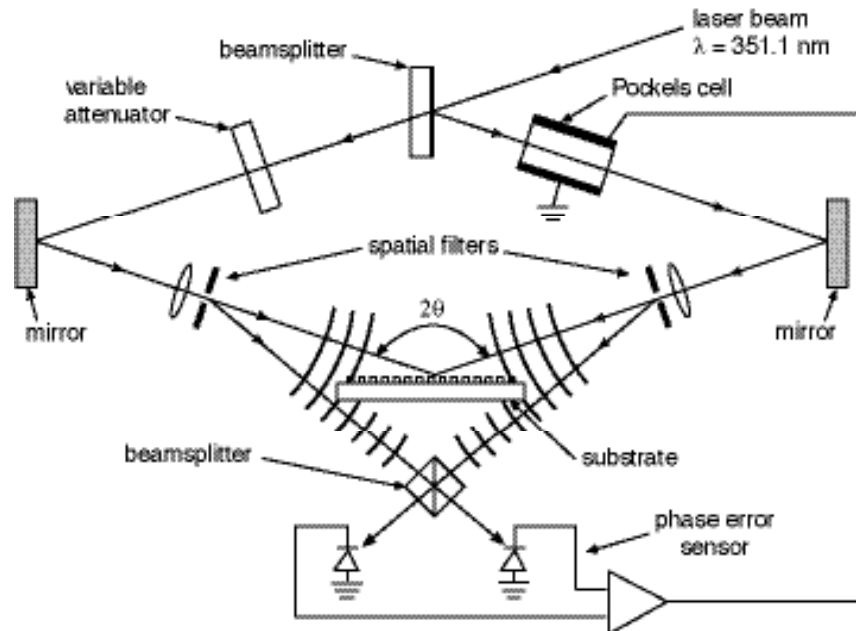


**Figure 1.** Schematic of the MIT interferometric lithography system. The system occupies a 2x3m optical bench in a class 100 clean environment. The beamsplitter directs portions of the two interfering spherical beams to photodiodes. A feedback locking is achieved by differentially amplifying the photodiode signals and applying a correction to the Pockels cell which phase shifts one of the beams.

This system is specially designed for high stability and repeatability and is capable of producing metrological quality gratings and grids up to 10 cm in diameter at spatial periods down to 200nm. Used primarily for satellite applications, gratings produced with this tool have flown on numerous missions, most notably, the Chandra x-ray astronomy satellite launched in August of 1999 which included hundreds of matched, high-precision gratings.

We operate another system similar to the one shown in Figure 1 based around the 325 nm line of a HeCd laser. This system functions both as an exposure tool with capabilities comparable to those described above as well as an analysis tool. Using a technique known as holographic phase-shifting interferometry (HPSI), the linearity and spatial phase of gratings produced in this system can be quantitatively measured and mapped with an accuracy on the order of parts per million. Known hyperbolic distortions in the spatial-phase of gratings printed using IL are responsible for changes in periodicity of a few angstroms (for a 200nm period grating) over a 10 cm wafer. Although seemingly small, distortions of this scale can be highly significant, especially in metrological applications such as the fiducial grids for spatial-phase locked electron-beam lithography. Using the HPSI, we have been able to investigate innovative techniques for reducing these distortion levels. One method, based on the controlled distortions of the substrate during exposure, has demonstrated a reduction of the distortion pattern from 2 dimensions to 1 dimension as well as reducing distortions by almost an order of magnitude. Grating periodicity for exposures on flat and optimized curved surfaces are shown in Figure 2. The periodicities are calculated for the interference of 1 meter radius spherical beams at  $\lambda=325$  nm with a nominal interference angle of 45 degrees.

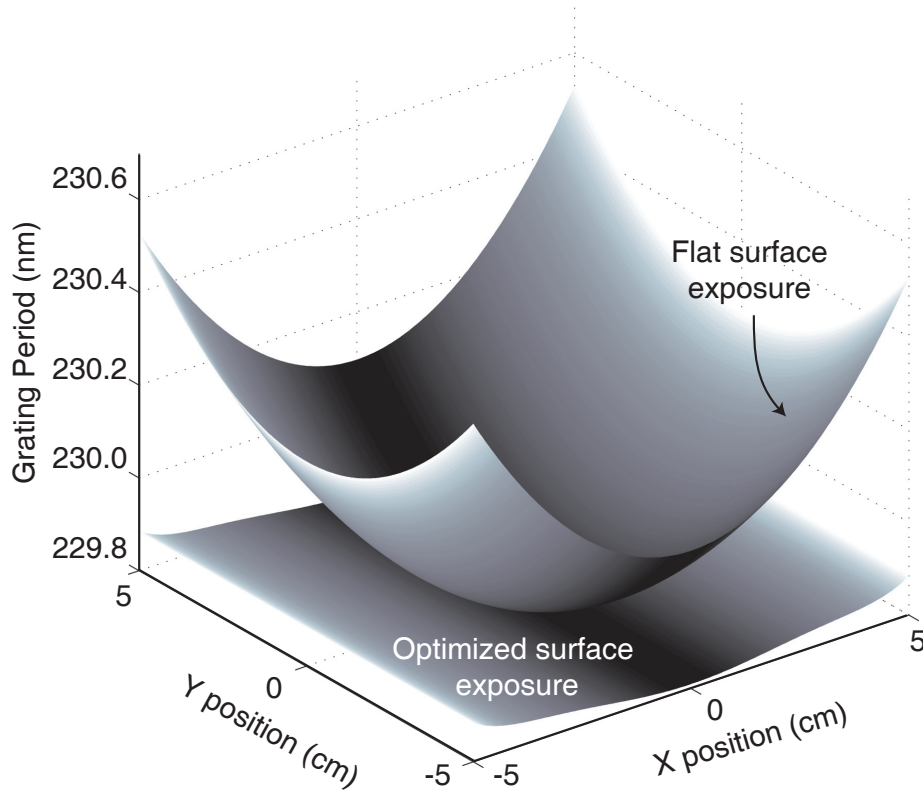


**Figure 2.** Periodicity of gratings exposed on a standard flat substrate and an optimized curved substrate. Notice that the grating period varies in both X and Y directions for the flat surface exposure, but only in the X-direction for the optimized exposure. Maximum variations are reduced by almost an order of magnitude.

Also utilizing a 325 nm HeCd laser is the Lloyds-mirror interferometer, shown schematically in Figure 3. This scheme is equivalent to half of the Mach-Zender configuration shown in Figure 1. A single point source is used in conjunction with a mirror placed normal to the substrate, which creates the image of a second source. The primary advantage of the Lloyds-mirror is that the spatial-period of the exposed gratings can be easily and continuously varied from many microns down to ~170 nm with an accuracy better than 1 part in 1000 without re-aligning the optical path. This has opened the door to new possibilities such as varied aspect ratio grids (different periodicities in the two axes of the grid) for patterned magnetic media and MRAM (magnetic random access memory) devices. Among the many other applications of IL supported by the Lloyds-mirror are alignment templates for organic crystals and block co-polymers, semiconductor quantum dots, and other self-assembling structures. Templates for the Templated Self Assembly (TSA) project are made using this equipment. Distributed feedback (DFB) structures for quantum dot lasers and photonic bandgap devices have also been made using the Lloyds mirror.

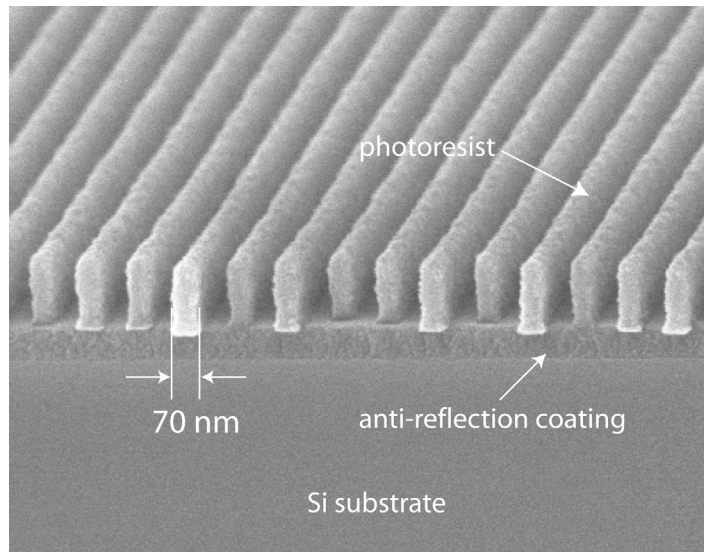
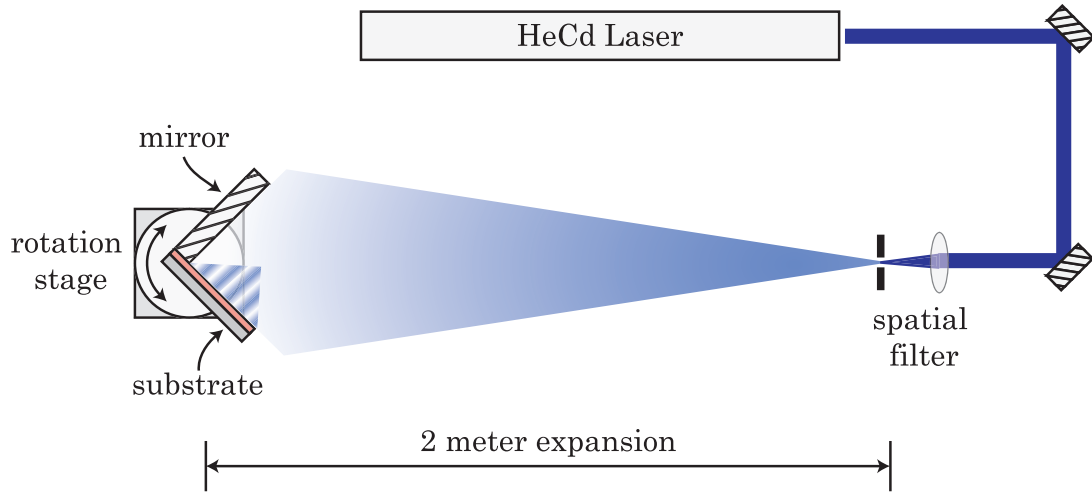


**Figure 3.** Schematic of a Lloyds-mirror interferometer. The substrate and mirror are fixed at a 90° angle to one another, and centered in a single incident beam. Rotating the substrate/mirror assembly as indicated varies the spatial-period of the exposed grating. The micrograph shows a grating with 70 nm lines on a 170 nm pitch exposed using the Lloyds-mirror.

For spatial periods of the order of 100 nm, we use a 193 nm ArF laser. To compensate for the limited temporal coherence of the source, we utilize an achromatic scheme shown in **Figure 4**. In this configuration the spatial period of the printed grating is dependent only on the period of the parent gratings, regardless of the wavelength and temporal coherence of the source. Thus, gratings and grids produced with this tool are extremely repeatable. **Figure 4** also shows a 100 nm-period grid of 13 nm-diameter posts etched into Si, produced with achromatic interferometric lithography (AIL) and a sequence of etching steps. Applications of AIL include patterned magnetic media, gratings for atom-beam interferometry, and templated self-assembly.

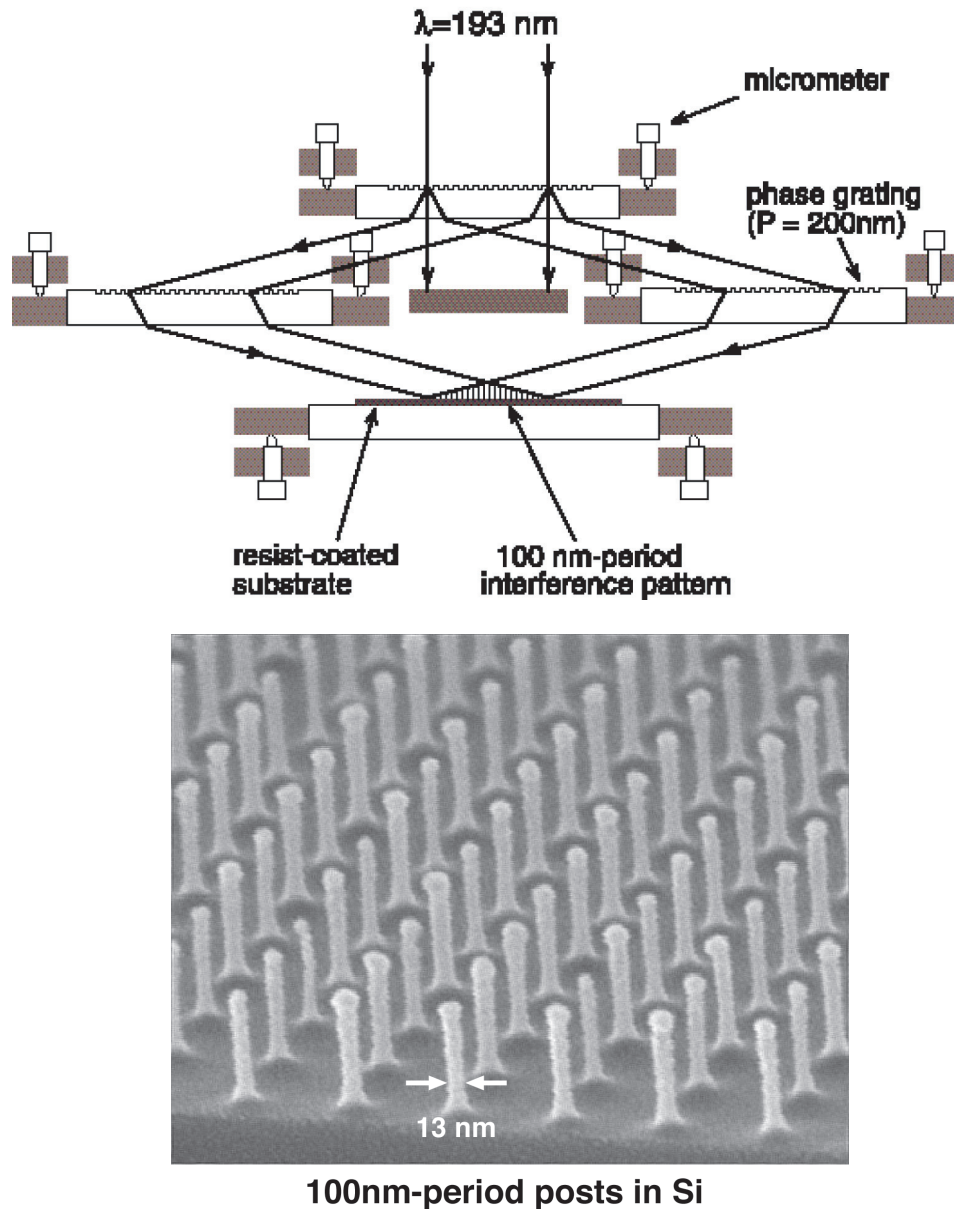


**Figure 4.** (Top) Achromatic interferometric lithography (AIL) configuration used to produce 100 nm-period gratings and grids. (Bottom) Scanning electron micrograph of a 100 nm-period grid, exposed in PMMA on top of an antireflection coating, and transferred into Si by reactive ion etching and  $\text{SiO}_2$  etching.

Using a grating-based achromatic interferometer, the period of the exposed grating is exactly half that of the parent gratings. This invites a "bootstrapping" technique where we use the 100 nm gratings made with the 193 nm AIL as parent gratings for 50 nm period exposures. We are currently developing a new generation of interference lithography tools to accomplish this. However, for a given wavelength, the smallest period possible is  $\lambda/2$ , which means that a photon source of  $\lambda < 100\text{ nm}$  is necessary for the next generation of tools. The limited availability of

sources, as well as poor optical properties of materials in this wavelength regime are major design obstacles. One option for circumventing both of these problems is to use immersion in a high-index medium to reduce the effective wavelength ( $\lambda_e$ ) of a source such as the 193 nm ArF laser, or a 157 nm F<sub>2</sub> laser. For example, in a medium with refractive index  $n=1.6$ , the effective wavelength of the ArF laser is  $\lambda_e = 121$  nm, and for the F<sub>2</sub> laser  $\lambda_e = 98$  nm. Thus, grating periodicities in the 50-60 nm range should be possible with currently available laser sources. We have demonstrated the use of immersion to enable exposures with periodicity below  $\lambda/2$ . Figure 5 shows a 90-nm period grating exposed via the spatial-frequency doubling of a 180 nm period parent grating using 193 nm light. We are currently working towards implementing this process at shorter periods. Other possibilities under investigation are free-standing gratings etched in a thin membrane for use with soft x-rays, or an analogous AIL scheme based on reflection gratings, which could be used on any wavelength despite high material absorption.

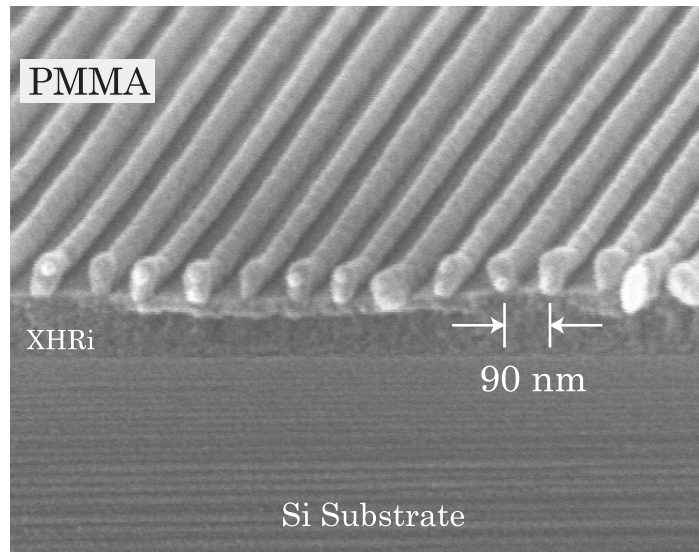


**Figure 5.** 90 nm period grating exposed in PMMA using 193 nm light in a medium with refractive index  $n=1.53$ . An anti-reflection coating (XHRi) is used between the substrate and the photoresist (PMMA) to improve the exposure profile.

## 10. The MIT Nanoruler: A Tool for Patterning Nano-Accurate Gratings.

### Sponsors:

NASA (NAG5-5405, NAG5-12583)

### Project Staff:

C.-H. Chang, C. Joo, Juan Montoya, Dr. Ralf Heilmann  
(Dr. Mark L. Schattenburg and Prof. Henry I. Smith)

Historically, the ability to observe and measure the results of processes has been critical to advancing fabrication technology. Thus, improvements in optical microscopy (e.g., Nomarski differential interference contrast) were a key enabler of the microelectronics revolution. In turn, the scanning-electron and atomic-force microscopes are essential tools as we move into the nanotechnology era. While the ability to print or resolve a particular feature size is a necessary condition for the successful lithographic manufacturing of nanosystems, it is, by no means, the only requirement. Equally important is the ability to measure and control the size and placement of lithographic features with very high accuracy

All modern lithographic production and inspection tools, and all precision tools for that matter, are based on the notion of a *metrology frame*. Such a frame is composed of three components: (1) a rigid mechanical structure, (2) means to measure the motion of a workpiece with respect to the metrology frame, and (3) means to project, image or detect patterns on the workpiece, such as by use of an optical or electron lens. The preferred means for measuring workpiece motion has been the laser interferometer. The accuracy of a lithographic tool is critically dependant on the accuracy of its metrology frame, which, in turn, is dependant on the accuracy of the interferometer. Due to a number of factors, however, interferometer accuracy is not keeping pace with the shrinking tolerances as called for by the semiconductor industry roadmap, and is inadequate for many integrated optoelectronic patterns and the future nanotechnology revolution.

To address this problem, we are developing a lithographic tool called the *Nanoruler* that is designed to pattern gratings of such high accuracy that they may serve as the means for detecting workpiece motion in precision tools, using a method known as optical encoding, with an accuracy that is some 10-100X better than laser interferometers. The Nanoruler utilizes a patterning method called *scanning-beam-interference lithography* (SBIL), developed in the Space Nanotechnology Laboratory (SNL), that is capable of rapidly patterning large gratings (>300 mm diameter) in only a few minutes with unprecedented accuracy (see Fig. 1). Such super-accurate gratings can serve as optical encoder plates. Another important application for the Nanoruler is the patterning of nano-accurate gratings necessary for locking an electron beam using a novel technique called spatial-phase locked electron beam lithography (SPLEBL) that is under development in the NanoStructures Laboratory (NSL) and described elsewhere.

High fidelity gratings are also critical for advanced instrumentation and optics such as laboratory and astronomical spectrographs, high-bandwidth optical communications and fusion energy research. Conventional means of fabricating gratings, such as diamond ruling, holography, or beam writing, can take many hours or weeks to complete, and typically produce gratings of poor spatial-phase fidelity.

The concept of SBIL is to combine the sub-1 nm displacement-measuring capability of laser interferometry to control a high-performance air-bearing stage, with the interference of narrow coherent beams, to produce coherent, large-area, linear gratings and grids. Our ultimate goal is to produce gratings with sub-nm distortion over areas many tens of centimeters in diameter. SBIL requires sophisticated environmental controls to mitigate the effects of disturbances such as acoustics, vibration, and air turbulence, and variations of temperature, pressure, and humidity. The system also features real-time measurement and control of optical phase using heterodyne

fringe detection, acousto-optic modulator phase locking and a high-speed digital signal processor (DSP) controller (see Fig. 2).

An important feature of SBIL is the ability to both write and read gratings with nanometer control of grating phase. We have demonstrated  $\sim 2$  nm  $3\sigma$  repeatability of the writing and reading process. Fig. 3 shows a photograph of a 300 mm-diameter wafer patterned with the Nanoruler.

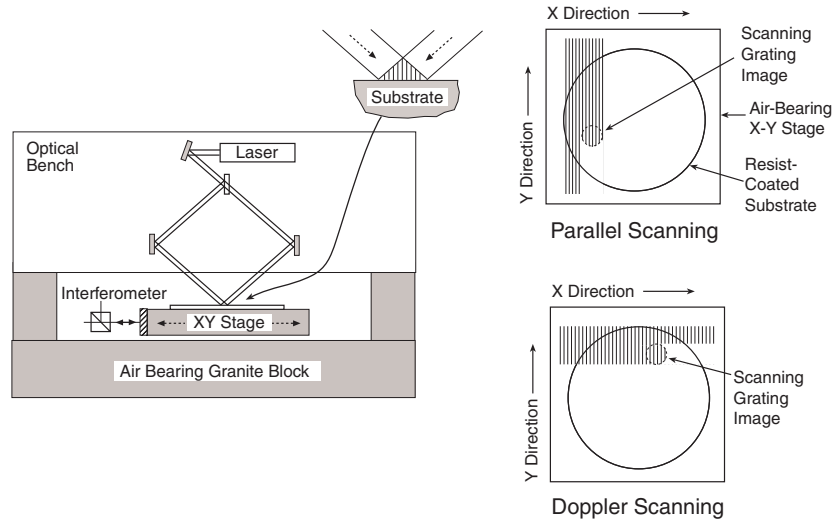


**Figure 1.** Schematic of the scanning-beam-interference lithography (SBIL) system under development in the SNL. A pair of narrow, low-distortion beams overlap and interfere at the substrate, producing a small grating “image.” The substrate is moved under the beams, writing a large area grating. Tightly overlapped scans ensure a uniform dose.

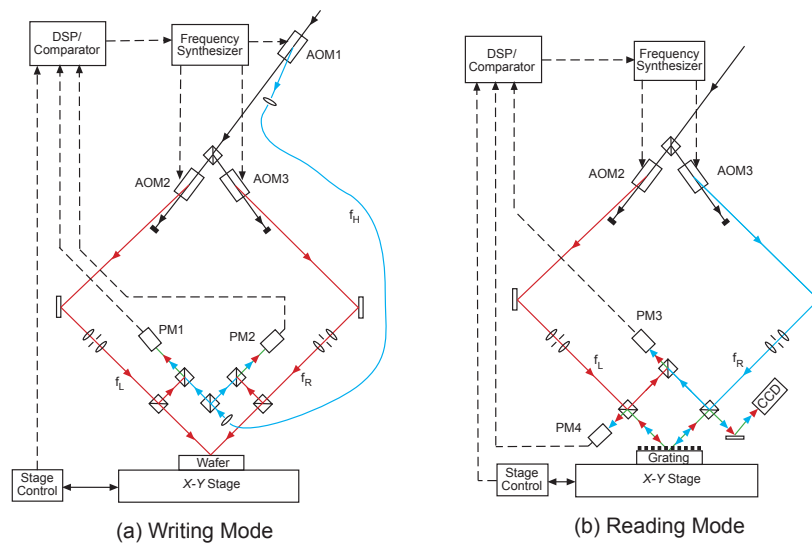


**Figure 2.** Schematic of SBIL acousto-optic (AO) modulator phase locking system. Both writing and reading modes are depicted. The phase of the grating image is measured by a small interferometer close to the writing surface. The AO modulators Doppler shift the beams into the mega-Hertz range, providing high-accuracy heterodyne measurement of phase. This information is processed by a digital signal processor and used to control RF frequency synthesizers which drive the AO modulators, thus locking the image phase to the moving substrate.

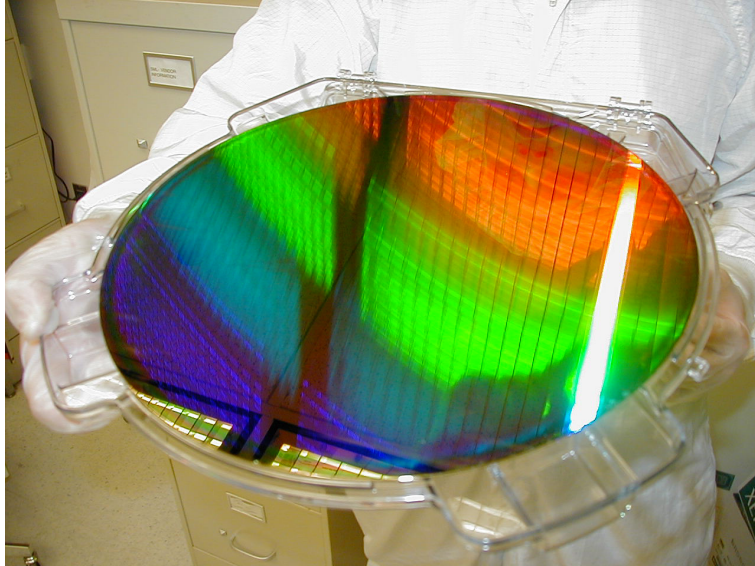


**Figure 3.** A 300 mm-diameter silicon wafer patterned with a 400 nm-period grating by the Nanoruler. The grating is diffracting light from the overhead fluorescent bulbs.

## 11. Interference Lithography for Patterning Variable-Period Gratings

### Sponsors:

NASA (Grants NAG5-5405, NAG5-12583)

### Project Staff:

C. Joo, J. Montoya, Dr. R. Heilmann, Dr. Mark L. Schattenburg

Scanning-beam interference lithography (SBIL) patterns large-area, linear, low-phase-distortion gratings with a pair of small diameter (millimeter size) phase-locked laser beams. We are developing a new system that generalizes the concept of phase-locked scanning beams for patterning continuously varying (chirped or quasi-periodic) patterns. These structures can subsequently be used to fabricate chirped x-ray reflection gratings for astronomical imaging applications, chirped fiber Bragg gratings for time-delay or spectral filtering applications, and/or diffractive optical elements.

Figure 1 shows the experimental diagram of the variable-period scanning-beam-interference lithography (VP-SBIL) system. For controlling the grating period and orientation, the system employs dual-axis picomotor-driven gimbal mirrors to produce symmetric deflections of a pair of interfering beams around the optical axis without translation. Two objective plano-convex lenses ( $f\# = 4.25, 2.12$ ) are used in a 4-f optical configuration. Such a lens system allows the conjugate points of beam deflection (on mirrors) to overlap at the focal plane of the second objective lens. The spot size of image overlap is reduced to half the beam diameter as the ratio of focal lengths  $f_2/f_1=0.5$ . This relaxes the maximum period variation ( $\Delta\Lambda$ ) constraint over the image diameter ( $D$ ) that requires  $\Delta\Lambda/\Lambda \ll \Lambda/D$  where  $\Lambda$  is the grating period.

To attain phase stability during grating patterning, homodyne fringe locking is adopted using an imaging detector, analog fringe-locker and a piezo-actuated mirror in closed-loop. In the present experimental configuration, two-axis beam rotation can generate any fringe orientation. However, variation in grating period ( $2 \mu\text{m}$  to  $1000 \mu\text{m}$ ) is limited by the range of deflection produced by the gimbal mirrors ( $\pm 10^\circ$ ) and by the numerical aperture (NA) of the lens system. Using position-sensitive detectors with an appropriate imaging and Fourier lens configuration, closed-loop beam steering is implemented to vary the grating period and orientation in a predetermined fashion. Typical requirements for x-ray reflection grating fabrication are  $\Lambda_{\text{ave}} \sim 2 \mu\text{m}$  and chirp factor  $\Delta\Lambda/\Lambda \sim 5\%$ .

Fig. 2 shows two grating images of period  $2.0 \mu\text{m}$  and  $4.0 \mu\text{m}$  obtained on a static substrate by changing the angle between the beams using the picomotor-controlled gimbal mirrors. Line uniformity in the images indicates minimal fringe distortion over the entire beam overlap. The picomotors can be constantly driven to write large-area gratings with continuously varying period and orientation on a substrate mounted to a precision X-Y stage. The piezo-actuated picomotors (which produce displacement jitter and exhibit low bandwidth operation) will be subsequently replaced by voice coil-actuated fast steering mirrors.

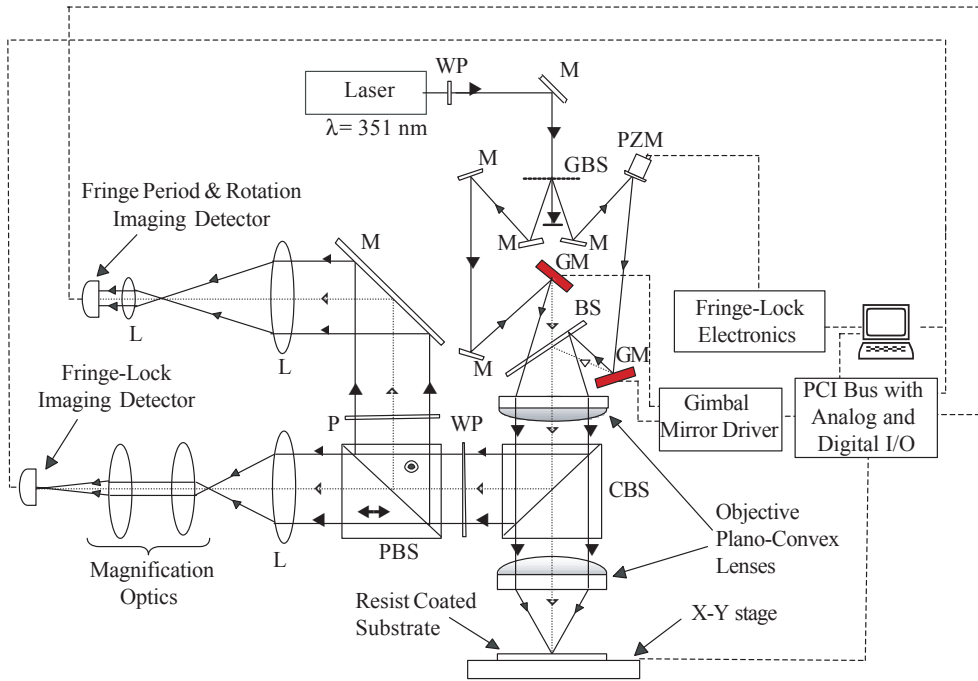


**Figure 1.** Experimental diagram of variable-period scanning-beam-interference lithography system. *M*: mirror, *L*: lens, *P*: polarizer, *GM*: gimbal mirror, *WP*: wave plate, *BS*: beam splitter, *PZM* piezo-actuated mirror, *GBS*: grating BS, *CBS*: cubic BS, *PBS*: polarizing BS.

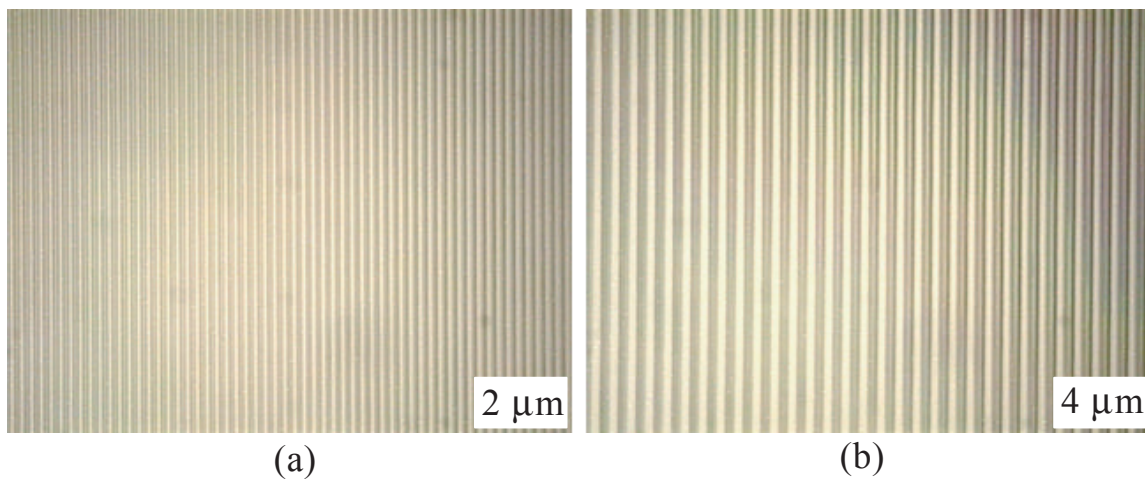


**Figure 2.** Optical micrographs of gratings written by VP-SBIL with periods (a)  $2.0 \mu\text{m}$  and (b)  $4.0 \mu\text{m}$ .

## 12. Precision Fabrication Techniques for Microphotonic Devices

### Sponsors:

Pirelli Lab S.p.A. Contract Number AGMT. DTD. 9/1/01

### Project Staff:

Tymon Barwicz, J. Todd Hastings, Milos A. Popovic, Peter T. Rakich, Michael R. Watts, Professor Hermann Haus, Professor Erich P. Ippen, and Professor Henry I. Smith.

Microphotonic devices seek to miniaturize and integrate the components needed for optical networking. These devices have exacting fabrication tolerances for feature size, pattern-placement, and surface roughness. Careful control of feature size is critical for resonant structures and phase-matching between coupled waveguides, while pattern-placement is essential for devices that rely on long-range interference effects. Surface roughness often dominates optical loss in a device. As a result, only careful control of the fabrication process can maximize device performance. This project focuses on Bragg-grating-based devices and high-index-contrast devices; both of which require precision fabrication.

### Grating-Based Devices

Bragg gratings have widespread application in the field of optical telecommunications. A Bragg grating is formed by creating a periodic corrugation or refractive index modulation in an optical waveguide. Such a structure behaves as a wavelength-selective filter, reflecting a narrow band of wavelengths while transmitting all other wavelengths. Although Bragg gratings are commonly imprinted in photosensitive optical fiber, physically-patterned gratings in planar waveguides, shown in figure 1, offer a number of advantages. For example, one can build Bragg gratings in non-photosensitive materials such as indium phosphide or silicon. In addition, integrated gratings can contain precise phase-shifts and variations in grating strength to achieve a desired filter response. Finally, the planar-fabrication process can integrate multiple gratings with splitters, couplers, and other optoelectronic components on a single, readily manufacturable chip.

We use a combination of several different types of lithography to generate Bragg-grating devices. In interference lithography, two coherent laser beams are crossed, generating a standing-wave interference pattern. This standing-wave pattern is used to expose photoresist, yielding a coherent submicron-period grating. This grating can be used directly as the device grating or it can serve as a precision reference for later electron-beam lithography steps.

For devices that require long Bragg gratings with engineered phase shifts or variations in grating strength, we use a technique called spatially-phase-locked e-beam lithography (SPLEBL), which combines the long-range spatial coherence of interference lithography with the flexibility of scanning e-beam lithography. Inherent pattern-placement errors in gratings written by standard e-beam lithography limit device performance. SPLEBL references the interference-generated grating during the e-beam exposure to minimize these placement errors.

In many cases, the techniques mentioned above are not applied directly to a device, but instead to an x-ray lithography mask. Once the mask is generated, with the appropriate gratings and alignment marks, the patterns can be repeatedly transferred to substrates using x-ray lithography.

One of the critical challenges facing integrated Bragg gratings is that they often require submicron grating structures patterned over relatively tall optical waveguides. In order to address this topography problem, we have developed a dual-hardmask process, depicted in Figure 2. This process allows both lithography steps to be performed over essentially planar surfaces. Figure 3 shows devices fabricated by the dual-hardmask process in the indium-phosphide and silicon-on-insulator materials systems.

In many cases it is desirable to place Bragg gratings in the sidewalls of optical waveguides as shown in Figure 1 (b). This technique allows the grating and waveguide to be patterned in the same lithographic step. As a result, the grating strength can be easily varied along the waveguide to introduce apodization. Apodization, the process of gradually increasing and then decreasing the grating strength, reduces side-lobe levels in the reflection and transmission spectra of the device, thus reducing cross-talk between neighboring channels in wavelength-division multiplexing. Figure 3 shows an apodized-sidewall grating in a SOI ridge waveguide along with measured transmission spectra. The waveguide-grating structures were patterned using spatial-phase-locked e-beam lithography (SPLEBL) and chlorine reactive-ion etching. The silicon-on-insulator substrates were provided by Canon.

### High Index-Contrast Devices

High-refractive-index-contrast-material systems enable very small bending radii in microphotonic devices. In low-index-contrast waveguides (such as optical fibers), the bending radii must be on the order of centimeters. On the other hand, integrated-optical waveguides exploiting the high index-contrast between silicon nitride and air may have bending radii below 10  $\mu\text{m}$ . This is 1000 times smaller. Consequently, device size shrinks considerably, and large-scale integrated optical circuits become possible. Unfortunately, fabrication of high-index-contrast devices is much more demanding than fabrication of low-index-contrast ones. The main challenges reside in precisely and accurately controlling dimensions of submicron features as well as in achieving the required smoothness of waveguide sidewalls. High-index-contrast devices are much more sensitive to feature size variations. Scattering losses due to sidewall roughness become increasingly important when index contrast goes up and often render devices unusable. In the NanoStructures Laboratory, dimensional control is addressed by using direct-write scanning-electron-beam lithography. The very high resolution allows for much better control of submicron features than photolithography. Moreover, sidewall roughness is addressed by optimizing the fabrication process and quantitatively measuring the spectral density of sidewall roughness responsible for scattering losses. The measuring technique is based on scanning-electron micrographs and has been developed in the NanoStructures Laboratory.

A cross-section of a smooth waveguide is presented on Figure 5. The high-index contrast between silicon-rich silicon nitride (SiN) and air is employed to achieve small bending loss in sharp bends. These waveguides are used to create channel add-drop filter based on optical ring-resonators (Figure 6). An add-drop filter redirects (drops) a particular telecommunication channel (particular wavelength) and replaces its content with new information (add) carried at the same frequency. This has to be done without disturbing the neighboring channels. In ring-resonator-based filters, light is evanescently coupled from a bus waveguide to the first ring. If the optical path in a ring is equal to an integer number of wavelengths, one has resonance. In this case, power carried at the resonant frequency of the rings will be entirely transferred from a bus waveguide (input) to the rings and then to the other bus waveguide (drop). The filter is symmetric and the add function is performed in a similar way. High-order filters are formed by cascading rings in series. A third-order-filter response is shown on Figure 7. It shows a wide free-spectral range of 24 nm (spectral distance between resonances) and a low input-to-drop-loss of 3 dB. The spectral asymmetry in the through port is due to resonant-frequency mismatch of the ring resonators. It will be corrected in future work to enhance the shape of the filter. The entire third-order filter covers about 35 by 35  $\mu\text{m}$  while low-index-contrast add-drop filters cover square millimeters or even centimeters.

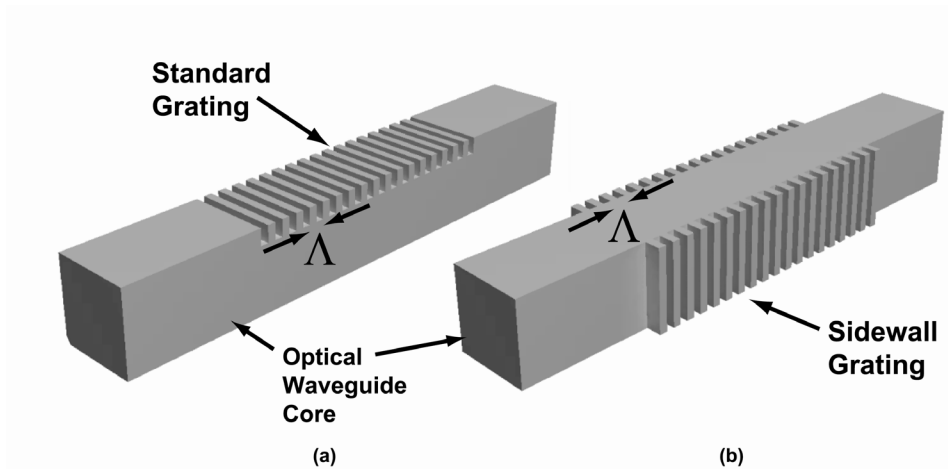


**Figure 1:** Two possible configurations for physically patterned Bragg gratings in optical waveguides. (a) Bragg grating patterned in the top of the high-index core. (b) Bragg grating patterned in the sides of the high-index core.

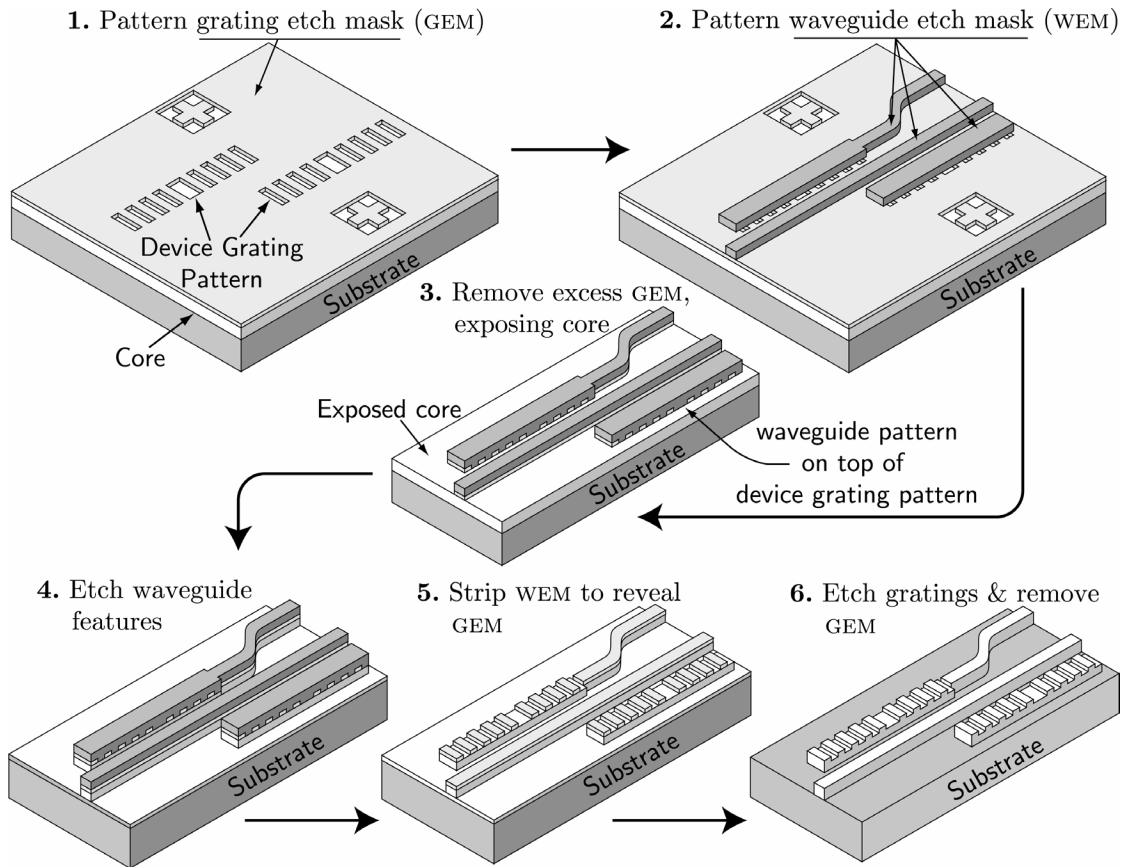


**Figure 2:** Dual-hardmask process used to pattern fine-period Bragg gratings atop relatively tall waveguide structures. The process is designed such that all lithography steps are performed over essentially planar topography.

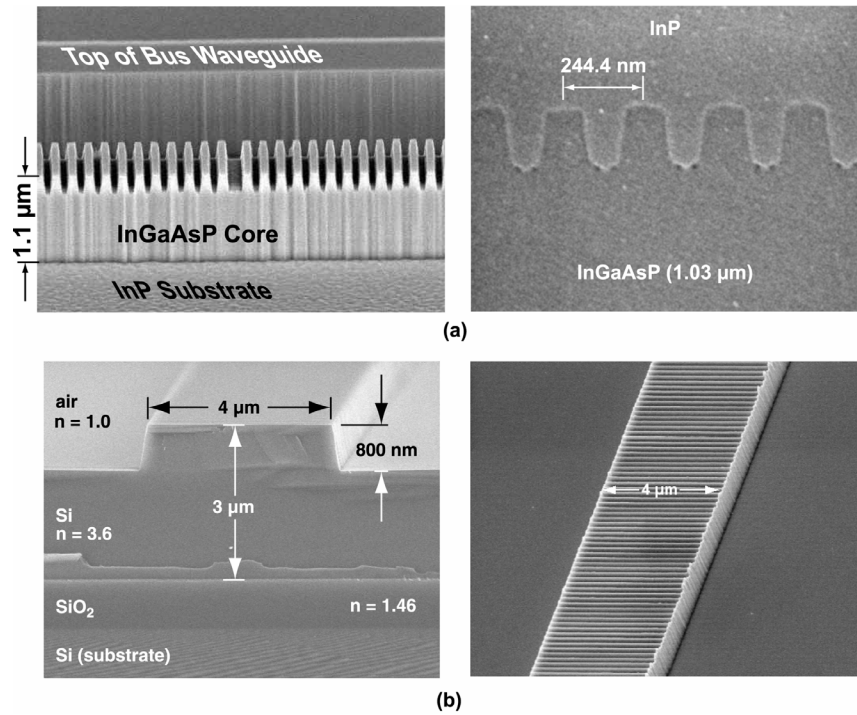


**Figure 3:** Examples of the dual-hardmask process applied to two different materials systems. (a) Scanning-electron micrograph depicting a quarter-wave-shifted, 244.4 nm period Bragg grating etched into the top surface of an InGaAsP waveguide, and the subsequent InP overgrowth. (b) Silicon-on-insulator (SOI) ridge waveguide cross-section and SOI waveguide with Bragg grating in the top.

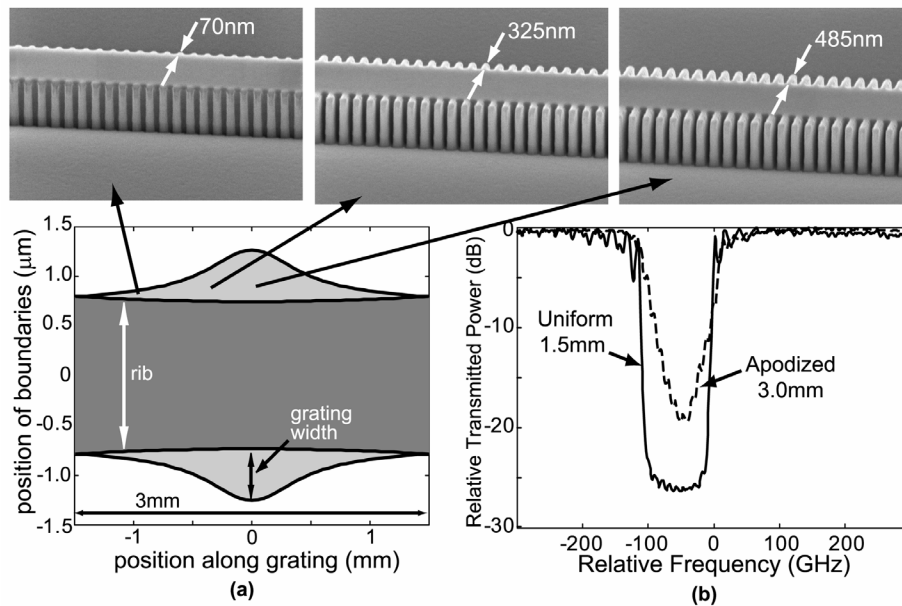


**Figure 4:** (a) Apodized Bragg gratings fabricated in the side-walls of a SOI ridge waveguide. (b) Transmission spectra for the TE- mode of uniform and apodized waveguide-grating devices. The reduction of side-lobe levels for the apodized devices is readily apparent.

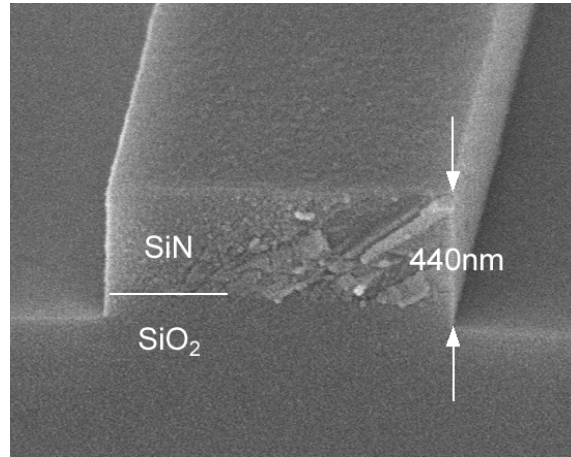


**Figure 5:** Cross-section of a high-index-contrast waveguide with smooth sidewalls. Light is guided by the 330-nm-thick silicon-rich silicon nitride (SiN) layer with an index of refraction of 2.20. The silicon oxide layer is about 3 microns thick and acts as optical isolation from the silicon wafer.

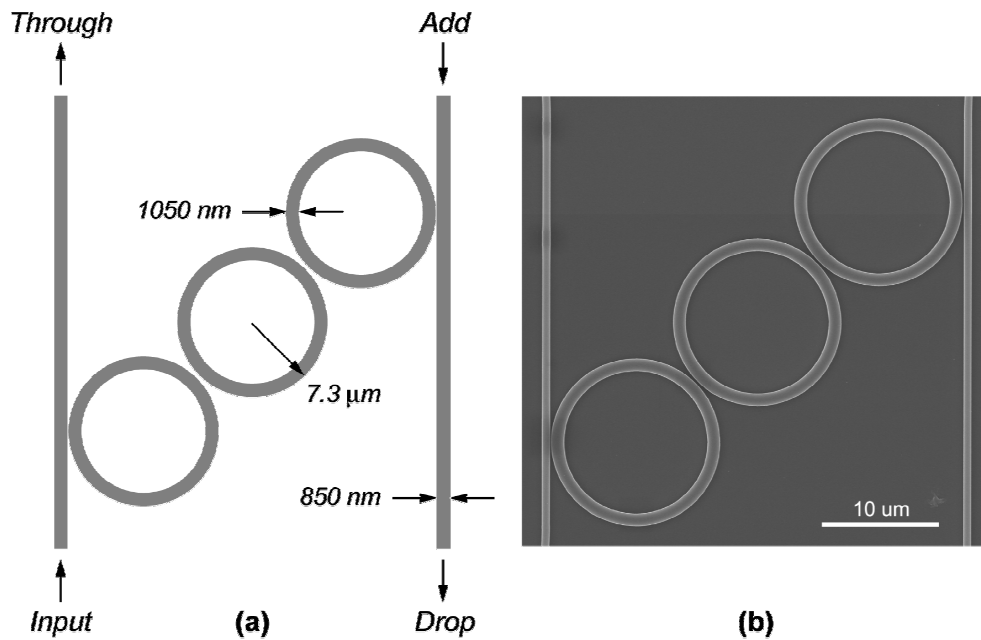


**Figure 6:** Third-order add-drop filter based on optical ring resonators. Designed filter on the left (a) and fabricated filter on the right (b). The coupling gaps between the bus waveguides and the outer rings are 60 nm. This structure was fabricated using scanning-electron-beam lithography. For high-volume manufacturing, a high-resolution replication technique such as nano-imprint or x-ray lithography could be used.

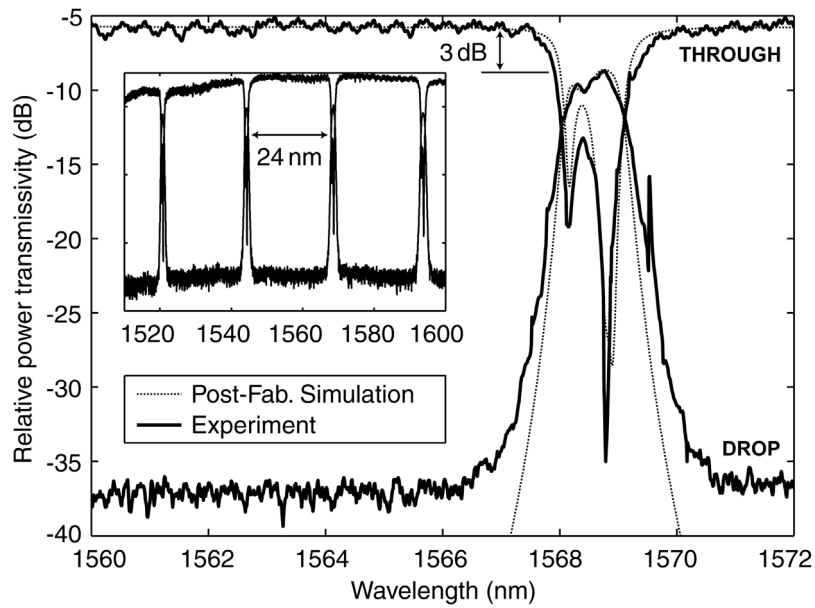


**Figure 7:** Spectral response of a third order add-drop filter based on optical ring resonators. Wide free-spectral-range of 24 nm and low 3 dB drop-loss are shown. Post fabrication simulations based on three-dimensional finite-difference-time-domain were performed using measured dimensions and refractive indices. Excellent agreement with experiment is observed considering that no parameter fitting was used except for the ring resonant frequencies. The spectral asymmetry is due to frequency mismatch of resonators and will be corrected in future work

### 13. Fabrication of 3-D Photonic Crystal (PhC) Structures

**Sponsors:**

National Science Foundation  
 Contract DMR-9808941

**Project Staff:**

Minghao Qi, Professor John Joannopoulos, Professor Henry I. Smith

Last year we reported the successful fabrication of a seven-layer 3D photonic crystal (Figure 1a). This year we introduced point defects into this crystal. With the layer-by-layer approach and the flexibility of scanning e-beam lithography, defects can be introduced in any of the crystal layers. In Figure 1a, a set of air holes, denoted as B', were not etched during the fabrication, thus forming point defects, or microcavities. Simulation shows that this type of defects has several modes and will have three resonances observable for normal excitations at 1.3, 1.4, and 1.5  $\mu\text{m}$ . The electric field magnitude at the resonance wavelength of 1.3  $\mu\text{m}$ , calculated and shown in Figure 1c, indicates that the defect mode is completely confined within the crystal, thus forming a microcavity. The fabrication procedures are the same as we reported in previous years and the finished photonic crystals are shown in Figure 2.

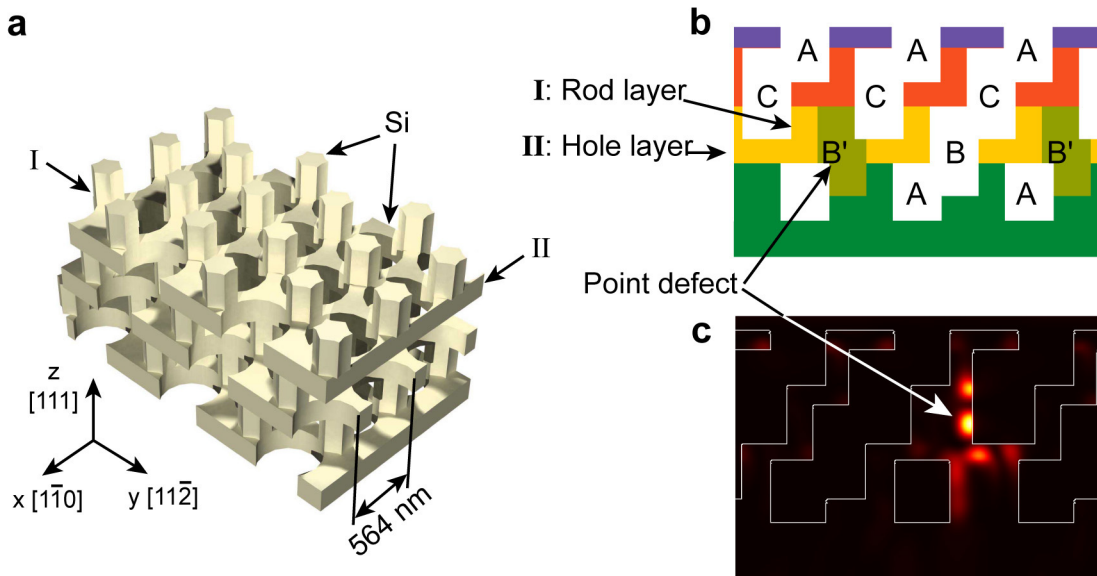


**Figure 1:** A schematic of the 3D photonic crystal (PhC) and the associated point defects. (a) computer rendering of the photonic crystal. (b) Cross-sectional view of the PhC along a plane determined by axes [111] and [1,1,-2]. The PhC can then be viewed as an fcc lattice of air cylinders (denoted ABCA) in high dielectric (Si). Two adjacent layers of air cylinders intersect with each other and the remaining Si at the intersection layer forms a rod layer. Cylinders denoted by B', if not etched during the fabrication, form so-called "dielectric" point-defects. (c) Mode profile of the defect state at 1.3  $\mu\text{m}$ , showing the majority of power is confined within the photonic crystal.

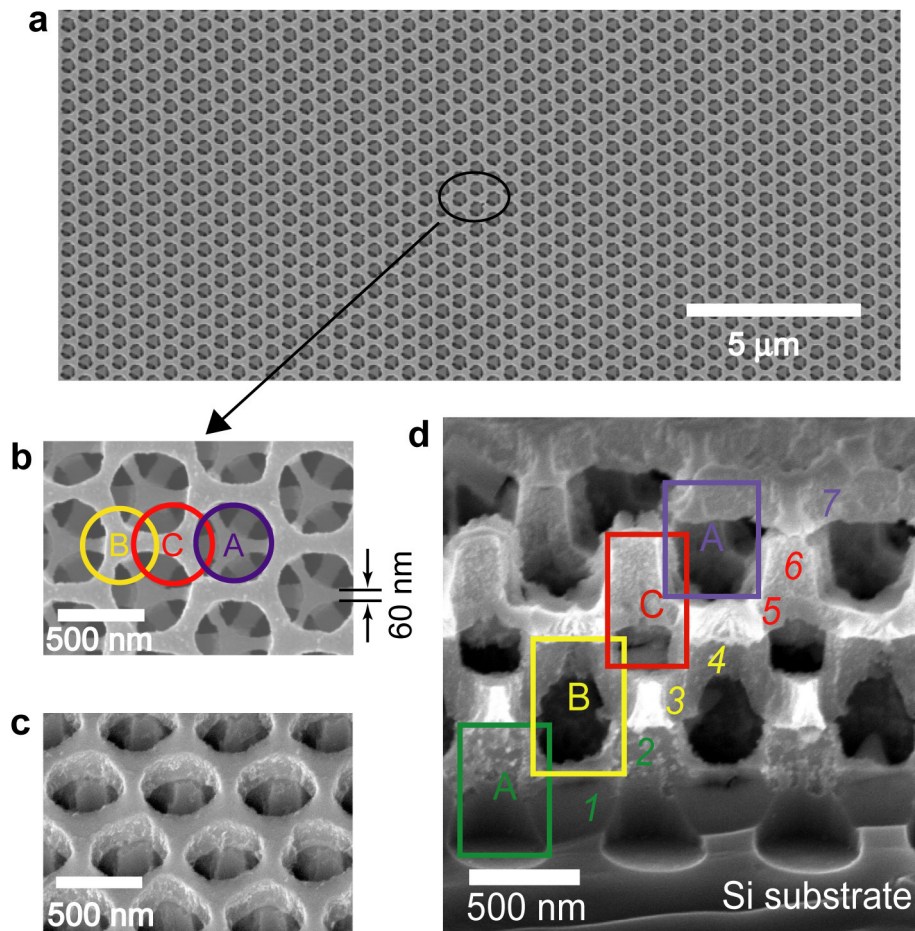
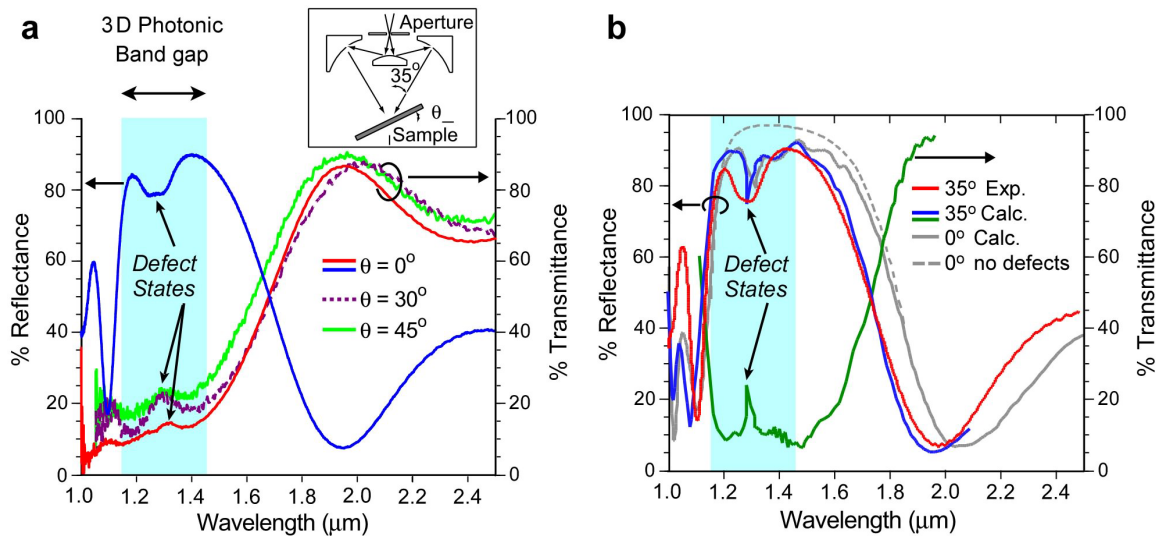


Figure 2: Scanning electron micrographs of the fabricated 3D photonic crystal. (a), Low magnification top view. (b), A close up showing the hexagonal array of holes, denoted by “A”, while “B” and “C” are the sets of holes underneath the top layer, showing a sequential shift in the horizontal direction. The rod layers are completely blocked by the hole-layers. (c), A tilted top view of the crystal reveals the rod layer. (d), A cross-sectional view. The functional layers are marked by numbers, while the etched holes (air cylinders) are outlined with rectangles. The crystals shown in (c) and (d) were fabricated at an earlier time than the one shown in (a) and (b).

To characterize the 3D bandgap and to identify the resonance modes of the point defects, we took the transmission and reflection spectra at room temperature with a Nicolet Fourier Transform Infrared (FTIR) microscope, whose bandwidth covers the entire bandgap. The unpolarized incident infrared light passes through a variable aperture, diverges to a hyperbolic reflecting mirror, and is then refocused to a small spot on the sample (Figure 3 inset). The incident light thus forms a cone-shaped bundle with a half angle of  $35^\circ$ . Such an illumination scheme includes incidences with various spatial orientation and polarization and is thus desirable for characterizing a 3D photonic band gap. The sample is located at the focal plane and can be tilted relative to the axis of the illumination cone. The aperture size was fixed so that the sample collection area was around  $30 \mu\text{m}$  by  $30 \mu\text{m}$ . The substrate Si wafer was double-side polished and the signal-to-noise ratio was high. For the transmission measurement, the reference was an area of bare Si adjacent

to the 3D PhC device. The sample was tilted from [111] toward [1,1, -2] for 30° and 45°. Reference measurements were taken for each tilt angle, and the spectra were normalized accordingly. For the reflection measurement, the reference was a freshly evaporated 1 $\mu$ m Gold film on a three-inch wafer. Figure 3a shows the transmission and reflection spectra of a typical 3D PhC.

The measurement shows consistent attenuation from 1.15  $\mu$ m to 1.6  $\mu$ m for sample tilt angles from 0° to 45°. Notice that for nonzero sample tilt angles, each recorded spectrum is actually an average over a variety of incident angles. For example, a transmission spectrum at 45° sample tilt includes incidence angles from 10° to 80°. Therefore, these results clearly demonstrate an omnidirectional photonic band gap. Another evidence of the photonic band gap is the fact that the reflectance  $R$  and transmittance  $T$  in the zero degree sample tilt (corresponding to a uniform 35° incidence with respect to the sample normal) add up to (100 $\pm$ 6)% for a wide frequency range from 1.21  $\mu$ m up to 2.45  $\mu$ m. For short wavelengths, we have more confidence in the reflection data than the transmission data because the light source is much weaker at those wavelengths and a thick substrate (0.5 mm) degrades the signal.



**Figure 3:** Optical properties of the PhC. (a), Reflection and Transmission spectra of a 3D PhC with point defects. The transmission spectra, shown in red, purple and green, were taken for sample tilt angles of 0°, 30° and 45°, while the reflection spectrum (blue) was take for 0° sample tilt only. Inset is the optical path of the FTIR microscope. For non-zero sample tilts, the spectrum is an average of a variety of incident angles, while for 0° sample tilt, the incident light beams have a uniform incident angle of 35° with respect to the sample normal. (b), Comparison of measurement and simulation for a 3D photonic crystal at 35° incident angle. The measured reflection spectrum is shown in red. The calculated reflection spectrum is shown in blue, and matches extremely well with the measurement in terms of defect state position, band gap region, and maximum/minimum reflectance. The calculated reflection spectrum (grey line) at normal incidence, though similar in general shape, has a slight shift of band gap region. The dashed line corresponds to the reflection of a 3D PhC with no defects. A transmission spectrum, shown in green, was calculated independently from the reflection spectra and is in good agreement with the experimental results in (a).

A clear broad defect signature can be observed at 1.3 $\mu$ m, around the middle of the 3D band gap, as a dip in the reflection and corresponding increase in transmission. This is consistent with theory that “dielectric” point defects pull down certain states from above the band gap, creating so-called defect states, which produce resonant transmission at their corresponding wavelength (in this case, 1.3  $\mu$ m) within the band gap. As a control experiment, a previously fabricated

structure without defects did not show such a dip in the band gap. Moreover, the positions of the resonance peaks, as shown in Figure 3a, are independent of excitation angle. Thus we can conclude that this dip is truly due to defect resonance. To our knowledge, this is the first direct experimental observation of defect states at such length scale in a 3D PhC. The difference in the signature of the defect states in the reflection and transmission spectra is also expected. An incident plane wave couples with the defect modes and gets re-emitted into all directions. This results in a loss in reflection but a smaller gain in transmission, since not all scattered light is collected in measurement.

To further investigate the defect states, the measured feature sizes of a fabricated 3D PhC were fed into a finite-difference time-domain (FDTD)20 simulation program to calculate the reflection and transmission spectra for a zero degree sample tilt. A comparison of measured and calculated spectra is shown in Figure 3b for a 35° incident angle. The peak position of the defect states and the bandgap region agree extremely well with the simulation. The wider linewidth of the defect states in the experimental data arises most probably from the unavoidable small structural variations of many individual defects. The maximum reflections for almost all the samples were measured to be ~ 90%, while the simulation gave a maximum reflection of 93%. This excellent agreement demonstrates the high quality of the fabricated PhC. Such agreement is particularly noteworthy since no empirical adjustments of any kind were made either to theory or experiment. The only input into the simulation was the set of measured feature sizes.

The demonstration of designed defect states in a 3D photonic crystal, together with a robust fabrication process for 3D nanostructures we proposed last year, should lead to more functional devices in the near future, and eventually to 3D optical integrated circuits.

### 14. Design and Fabrication of a Superprism Using Two Dimensional Photonic Crystals

**Sponsors:**

Rockwell Science Center, contract #B1F431652

**Project Staff:**

Sheila Tandon, Chiyun Luo, Dr. Gale S. Petrich, Prof. Leslie A. Kolodziejski, Prof. Henry I Smith, and Prof. John D. Joannopoulos

A superprism is an optical device similar to a conventional prism but with two enhanced properties: (1) super-dispersion and (2) ultra-refraction. Just as a conventional prism separates light into multiple wavelengths, a superprism separates these wavelengths over wider angles--termed "super-dispersion." A superprism can also be used to magnify the angle of propagation of a single wavelength of light to steer the beam over wide angles--termed "ultra-refraction." The superprism effect depends on photonic crystal phenomena. Superprism effects have a number of applications ranging from enhanced devices for wavelength division multiplexed (WDM) systems to a new class of ultra-refractive optical elements for beam manipulation.

The device consists of a 2D photonic crystal with a square lattice of cylindrical air holes in a high-index material such as silicon or gallium arsenide. A top view schematic of the device shape is shown in Figure 1. The device is hexagonal shaped with the photonic crystal (PC) occupying a square region in the center. The input and output facets are indicated. The initial design has focused on realizing ultra-refraction such that an input angular sweep of approximately +/- 2 degrees is amplified to about +/- 30 degrees at the output, for a wavelength of 3.2 μm. The thick low-index layer is used to minimize radiation loss into the high-index substrate.

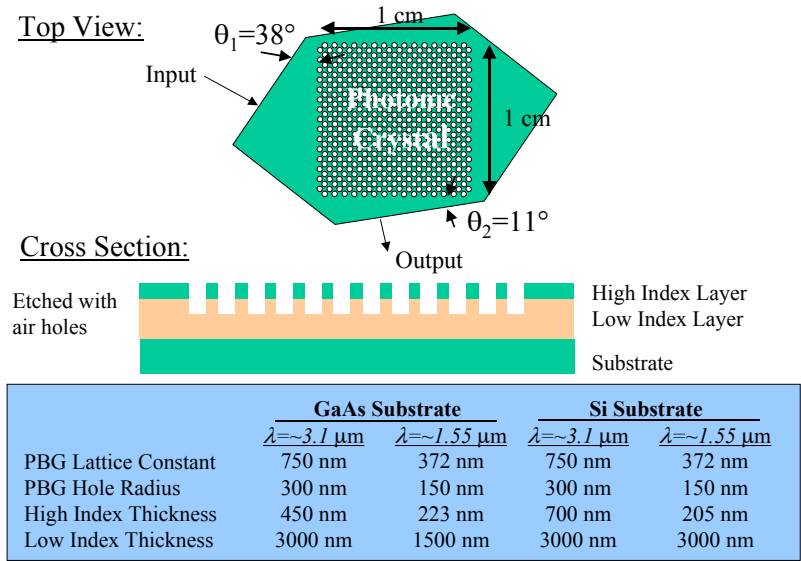
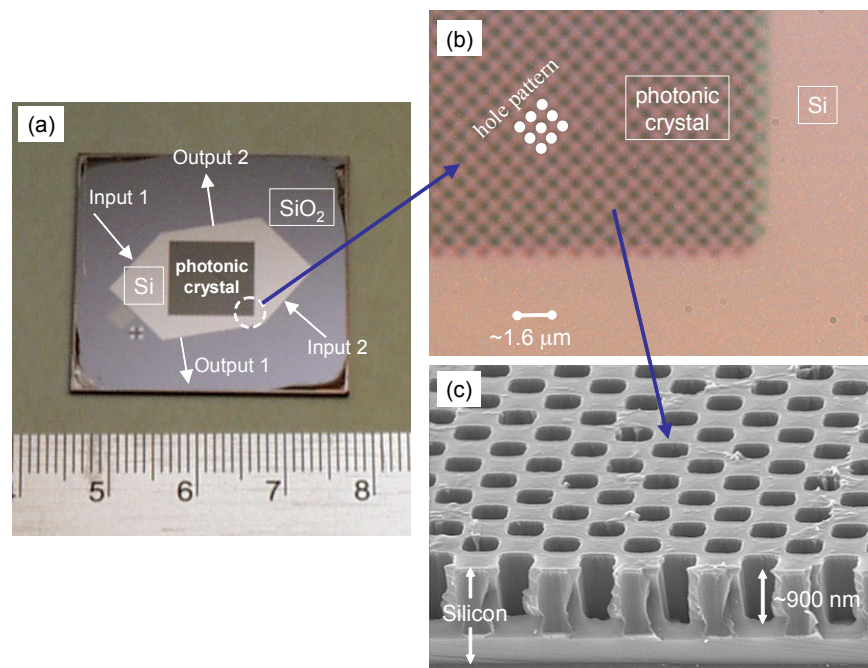


Figure 1: Superprism device design showing top and side views.

The feature sizes of the photonic crystal can be scaled depending on the material and the wavelength of operation, as shown in Figure 1. Our desired wavelengths of 3.1μm and 1.55μm imply hole lattice constants of 750nm and 372nm, and hole radii of 300nm and 150nm, in GaAs. The total thickness of the device (excluding substrate) is about 3.5 microns (460nm GaAs, 3mm Al<sub>x</sub>O<sub>y</sub>) while the top surface will have an area of about 2x2cm.

The hexagonal device shape is patterned using photolithography while the photonic crystal holes are patterned using interference lithography. After each lithography step, patterns are etched into hard-mask layers via reactive-ion etching (RIE). The fully patterned hard-mask layers are then used to etch the substrate material via another RIE step.

Figure 2 shows images of the fabricated device. In Figure 2(a), the full device is shown with its input and output facets indicated. The photonic crystal occupies the square region, and in Figure 2(b) a magnified plan-view of the corner area is shown. Figure 2(b) illustrates that very high alignment accuracy was achieved during the interference lithography step so that a line of holes was aligned to the square region with an error less than  $1^\circ$ . Figure 2(c) then shows an SEM micrograph of the cross-section of a silicon monitor sample that was processed in parallel with the fabricated device. The cross-section shows the air holes etched in silicon with a depth of 900 nm.



**Figure 2:** Images of fabricated superprism device. (a) Digital photograph showing full sample. (b) Nomarski Differential Interference Contrast image showing magnified corner area of the photonic crystal. (c) SEM micrograph showing cross-sectional image of a Si monitor sample.

Future work will focus on exploring issues related to coupling light into and out of the superprism. Some modifications of the current design will be needed to allow light to more effectively enter the device, excite the photonic crystal, and exit.

## 15. Coupling into Photonic Crystal Waveguides

### Sponsors:

National Science Foundation, Contract # DMR-02-13282

### Project Staff:

Solomon Assefa, P. Rakich, Dr. P. Bienstman, Dr. Steven G. Johnson, Dr. Gale S. Petrich, Professor John D. Joannopoulos, Professor Leslie A. Kolodziejski, Professor Erich Ippen, and Professor Henry I Smith

Large-scale photonic integrated circuits require guiding light around sharp bends with a radius of curvature on the order of a wavelength. In conventional index-guided waveguides, light is confined as a result of total internal reflection at the interface between the high refractive index waveguiding layer and its low index surroundings. However, using these conventional high-index-contrast waveguides in integrated circuits would be difficult because they are susceptible to large optical losses as the bend's radius of curvature decreases. Photonic crystals (PCs), which consist of a periodic arrangement of high and low-index dielectric material, have been proposed as a potential solution in order to guide light around corners with near perfect transmission, including  $90^\circ$  bends.

The 2D photonic crystal consists of an array of cylindrical rods of high dielectric-constant material above a low-dielectric-constant material. Introducing a line defect, such as a row of smaller radius cylinders, into the 2D photonic crystal results in a linear waveguide. The forest of periodic dielectric rods surrounding the line defect creates a photonic band gap (PBG), i.e. a range of frequencies in which light cannot propagate. Thus, an optical signal with a frequency inside the PBG has its energy confined within the line defect and becomes evanescent into the photonic crystal. The radius of the cylinders in the line defect remains large enough to provide index guiding in the third dimension (normal to the plane of periodicity). The localization of a mode inside the line defect can be utilized to guide light around sharp corners including a  $90^\circ$  bend with low optical loss. This is illustrated in Figure 1.

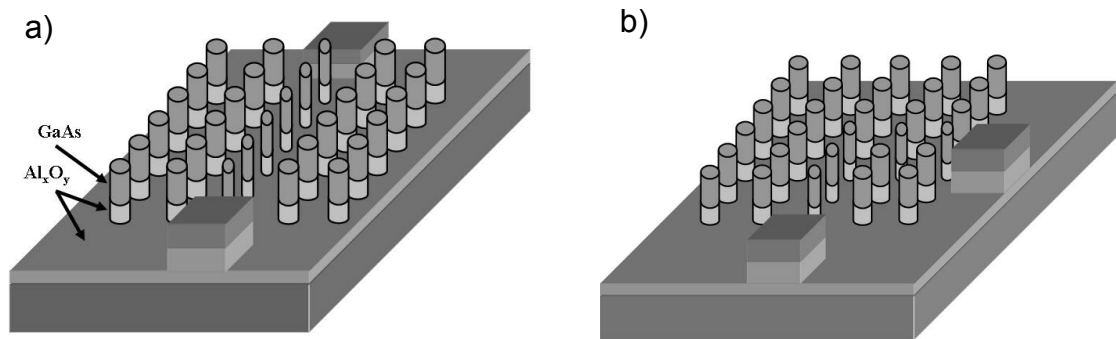


**Figure 1** (a) Schematic of a linear PC waveguide. (b) Schematic of a 90°-bend PC waveguide.

Nevertheless, the practical use of photonic crystal waveguides is limited due to the poor coupling efficiency between the photonic crystal waveguide, and conventional index-guided input and output waveguides. Coupling poses a challenge because the photonic crystal waveguide exhibits a significantly different mode profile and propagation mechanism compared to traditional waveguides that use index confinement. In the conventional waveguide the field has only forward propagating components, while the field in the photonic crystal waveguide has both forward and backward propagating components due to diffraction. Furthermore, guiding in the conventional waveguide is in high index surrounded by low index; in the photonic-crystal waveguide, guiding is in low index surrounded by two photonic-crystal “mirrors”.

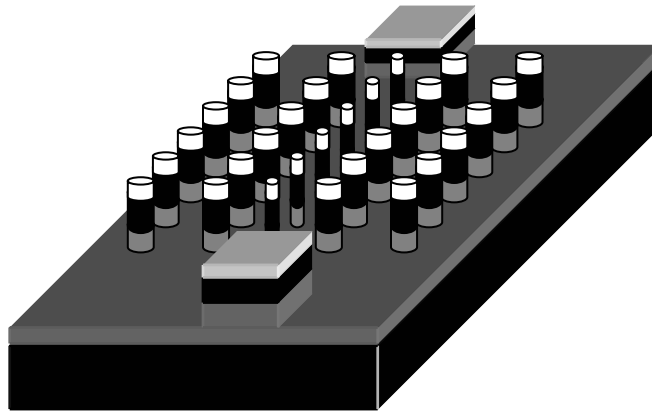
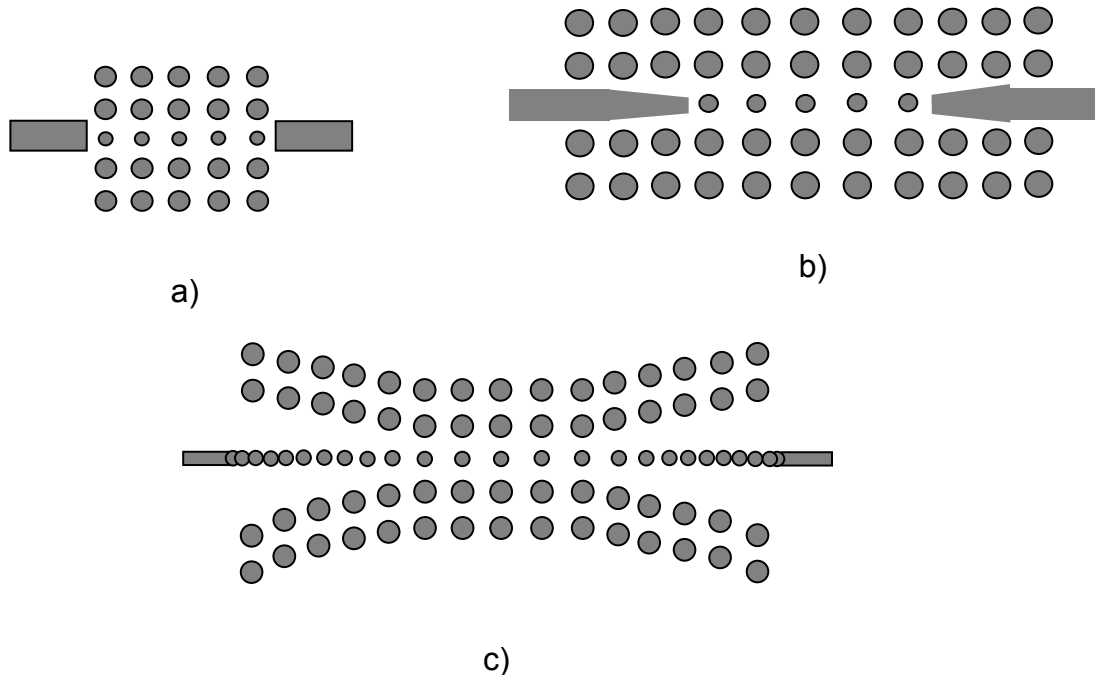


Figure 2 compares three different designs for coupling into the photonic-crystal waveguide. The design in Figure 2a suffers from Fabry-Perot reflection at the edges of the photonic crystal region, which makes the transmission of the waveguide dependent on the waveguide length. By tapering the end of input and output index waveguides as shown in Figure 2b, the reflection can be somewhat reduced. In the third design, the input waveguide is adiabatically converted into a strongly coupled cavity waveguide (CCW). This adiabatically transforms the forward propagating component of the field into both forward and backward propagating components before reaching the photonic crystal. Also, the cladding is introduced slowly from the edge, thereby adiabatically

transforming the mode from high-index guiding to gap guiding. 2D simulations show that this coupling scheme results in almost 100% transmission through the photonic crystal waveguide.



**Figure 2.** a) Schematic of coupling from an untapered dielectric waveguide. b) Schematic of coupling from a tapered dielectric waveguide. c) Schematic of an adiabatic transition from a dielectric waveguide into strongly coupled cavities and tapered cladding.

The cylindrical rods of the photonic crystal consist of a 550nm thick high-index epitaxial GaAs layer and 800nm thick low-index  $Al_xO_y$  layer. An additional 600nm thick  $Al_xO_y$  spacer layer is below the cylindrical rods isolating the GaAs guiding layer from the GaAs substrate. The heterostructure is grown using gas source molecular beam epitaxy on a (100) GaAs substrate. The  $Al_xO_y$  is initially grown epitaxially as  $Al_{0.9}Ga_{0.1}As$ .

The fabrication process commences by sputtering 300nm-thick  $SiO_2$  on the sample. Next, the waveguide and photonic crystal are defined using direct-write electron-beam lithography. Each sample is coated with polymethylmethacrylate (PMMA) electron beam resist, and each cylinder is defined by exposing a square pattern. The finite width of the beam rounds-off the corners of each square yielding a circular hole upon development. Simulations show that the largest band gap is obtained from a periodic arrangement of rods with diameter of 300nm. Exposure-dose experiments are done to find the optimal parameters for the exposures. A dose of  $536 \mu C/cm^2$ , current of 250pA, and clock frequency of 200 k Hz yields holes with a diameter close to the desired value. The input and output coupling waveguides and arrays of holes are written by stitching together  $250\mu m$  fields in the e-beam lithography.

A 40nm-thick nickel film is evaporated on the sample after the PMMA is developed, and a liftoff process is performed. The pattern is transferred to the SiO<sub>2</sub> by reactive-ion etching (RIE) in a CHF<sub>3</sub> plasma after which the nickel mask is removed using nickel etchant. Using the SiO<sub>2</sub> mask, the cylindrical rods are created by etching the GaAs and the AlGaAs to a total depth of 1.5 μm in a BCl<sub>3</sub>/He plasma. Next, each sample is cleaved in order to create a smooth input facet to promote the efficient coupling of a test signal of 1.55μm wavelength. Finally, the AlGaAs is transformed into Al<sub>x</sub>O<sub>y</sub> using a wet thermal oxidation process.

To optically test the devices, light is launched into the GaAs slab using a fiber and input coupler, and the signal from the output is analyzed with a photodiode. The transmission measured through the bulk photonic crystal is shown in Fig. 3(c); the bandgap ranges from 1448 to 1482 nm. Employing the two-stage coupling scheme, transmission versus wavelength for the photonic crystal waveguide is shown in Fig. 4(c). The measured result demonstrates guiding of light inside the bandgap of the surrounding bulk photonic crystal.

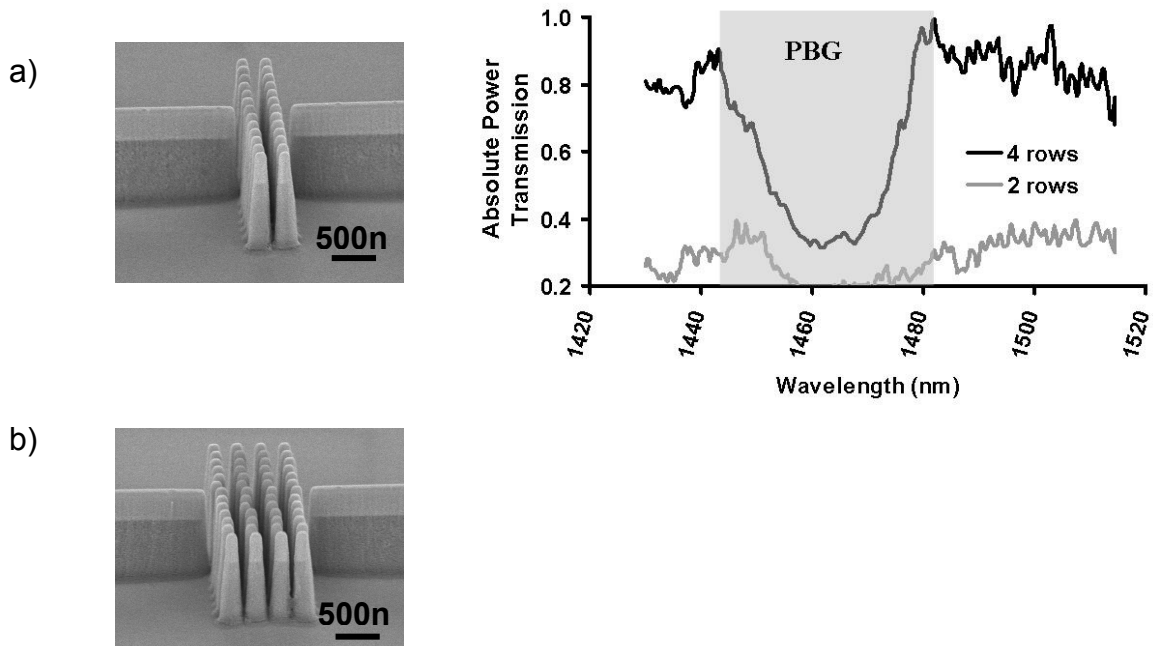


**Figure 3.** (a) Scanning Electron Micrograph (SEM) of photonic crystal with 2 rows of dielectric pillars (b) SEM of a photonic crystal with 4 rows of dielectric pillars (c) transmission measurement through the two structures.

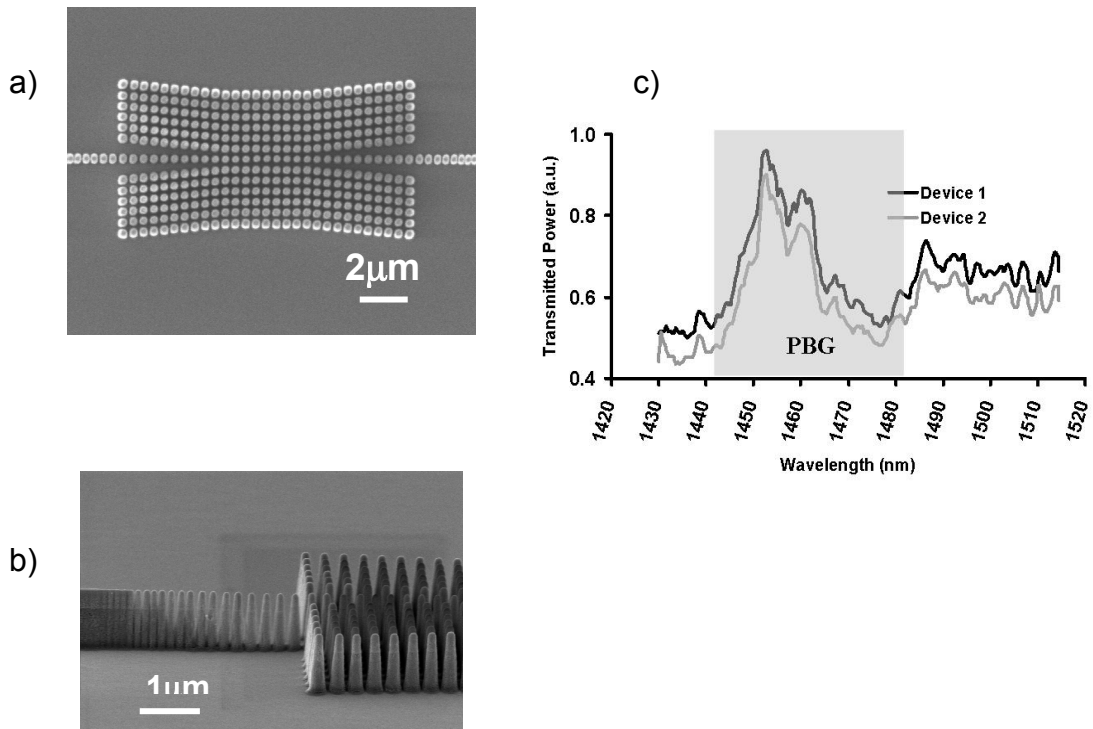


**Figure 4.** (a) Top-down SEM image of tapered photonic crystal waveguide (b) Side view SEM of tapered photonic crystal waveguide (c) transmission measurement through the structures in (a) and (b). Two PC waveguides fabricated on the same chip demonstrated similar transmission.